iScience

CellPress

Article

Molybdenum Nitride Nanocrystals Anchored on Phosphorus-Incorporated Carbon Fabric as a Negative Electrode for High-Performance Asymmetric Pseudocapacitor

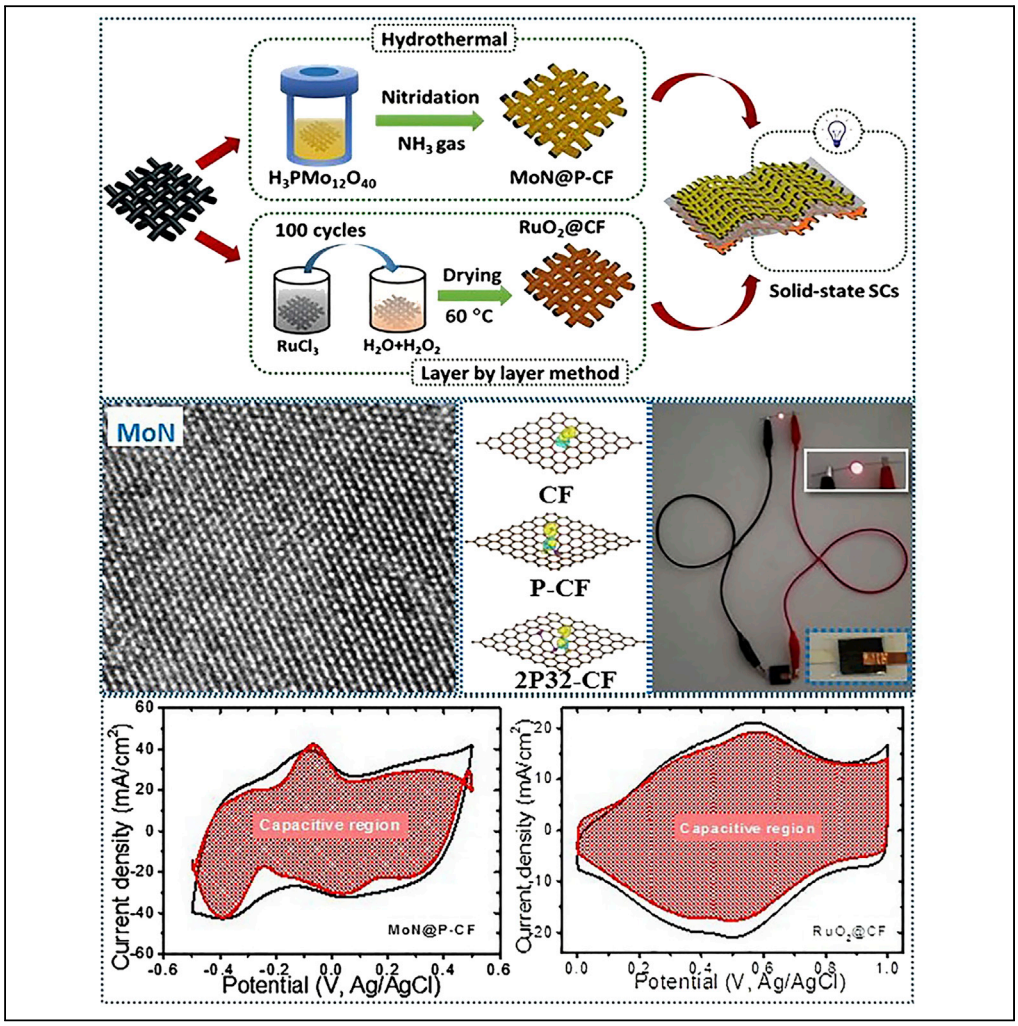

Deepak P. Dubal, Safwat Abdel-Azeim, Nilesh R. Chodankar, Young-Kyu Han

dubaldeepak2@gmail.com

HIGHLIGHTS

MoN nanocrystals coated on P-doped CF are used as high-performance pseudocapacitors

DFT simulations explain the origin of the good performance of MoN@P-CF electrode

MoN@P-CF and RuO_2@CF serve as negative and positive electrodes, in asymmetric SC

All-pseudocapacitive ASC delivers high power density with long cycling stability

Dubal et al., iScience *16*, 50–62
June 28, 2019
https://doi.org/10.1016/j.isci.2019.05.018

iScience

CellPress

Article

Molybdenum Nitride Nanocrystals Anchored on Phosphorus-Incorporated Carbon Fabric as a Negative Electrode for High-Performance Asymmetric Pseudocapacitor

Deepak P. Dubal,[1,4,*] Safwat Abdel-Azeim,[2] Nilesh R. Chodankar,[3] and Young-Kyu Han[3]

SUMMARY

Pseudocapacitors hold great promise to provide high energy-storing capacity; however, their capacitances are still far below their theoretical values and they deliver much lower power than the traditional electric double-layer capacitors due to poor ionic accessibility. Here, we have engineered MoN nanoparticles as pseudocapacitive material on phosphorus-incorporated carbon fabric with enhanced ionic affinity and thermodynamic stability. This nanocomposite boosts surface redox kinetics, leading to pseudocapacitance of 400 mF/cm^2 (2-fold higher than that of molybdenum nitride-based electrodes) with rapid charge-discharge rates. Density functional theory simulations are used to explain the origin of the good performance of MoN@P-CF in proton-based aqueous electrolytes. Finally, an all-pseudocapacitive solid-state asymmetric cell was assembled using MoN@P-CF and RuO_2 (RuO_2@CF) as negative and positive electrodes, respectively, which delivered good energy density with low relaxation time constant (τ_0) of 13 ms (significantly lower than that of carbon-based supercapacitors).

INTRODUCTION

Electrochemical energy storage (EES) devices such as supercapacitors (SCs) and Li-ion batteries are the primary choices for the majority of advanced applications ranging from implantable medical devices to electrical and hybrid vehicles (Dubal et al., 2015, 2018; Ko et al., 2017; Nam et al., 2006). The energy and power densities of EES systems define their utility in commercial applications, and these parameters are associated with charge-storing mechanisms. For instance, battery system offers high energy density due to the reversible redox reactions associated with the intercalation of alkali metal ions in the bulk of electrode; however, it is limited by very slow discharge-charge rates (Nitta et al., 2015; Yuan et al., 2017). Conversely, SCs (mainly conventional electric double-layer capacitor [EDLC] based) provide high power density, robust lifetimes, and safe operation, but are restricted by the low energy storage capacity (Salanne et al., 2016; Borenstein et al., 2017). Apart from them, pseudocapacitors, a subclass of SCs can be considered as a promising device, which exhibit high energy and high power densities in a single system, thus bridging the gap between batteries and SCs (Augustyn et al., 2014; Eftekhari and Mohamedi, 2015). Principally, pseudocapacitors store charges through fast and reversible surface redox reactions or intercalation pseudocapacitance. Typically, transition metal oxide or hydroxides, sulfides, and conducting polymers show pseudocapacitive behavior. Nevertheless, the poor electrical conductivity and the cycling stability of current pseudocapacitive materials hamper their practical applications (Wang et al., 2012; Yu and Lou, 2018). Therefore new pseudocapacitive materials with new cell designs need to be explored to achieve high energy and high power densities with good cycling stability to satisfy the increasing demands of energy storage systems.

Transition metal nitrides have recently attracted great attention as a potential electrode material for SCs due to their pseudocapacitive behavior, high reversibility, metallic electrical conductivity, and high chemical stability (Balogun et al., 2017; Yang et al., 2016). For example, the electrical conductivity of titanium nitride is in the range of 10^3 to 10^4 S/cm, which is close to that of metal and thus, beneficial for SCs (Lu et al., 2012). In the past, different metal nitrides such as TiN, VN, Mo_2N, and FeN have been explored as promising electrode materials for SCs (Balogun et al., 2015). Among these metal nitrides, molybdenum nitride (MoN) is one of the most promising pseudocapacitive material as it shows electrochemical features

[1]School of Chemistry, Physics and Mechanical Engineering, Queensland University of Technology (QUT), 2 George Street, Brisbane, QLD 4001, Australia

[2]Center of Integrative Petroleum Research (CIPR), College of Petroleum Engineering and Geosciences, King Fahd University of Petroleum and Minerals (KFUPM), Dhahran 31261, Saudi Arabia

[3]Department of Energy and Materials Engineering, Dongguk University-Seoul, Seoul 04620, Republic of Korea

[4]Lead Contact

*Correspondence: dubaldeepak2@gmail.com

https://doi.org/10.1016/j.isci.2019.05.018

similar to those of ruthenium oxide (Liu et al., 1998). However, the smaller electrochemical potential window (~0.6 V) and low capacitance of MoN-based pseudocapacitors limits their commercial utilization. Certainly, it is crucial to develop an adequate method to engineer MoN-based electrodes to achieve the desired electrochemical features.

An emerging strategy to extend the operational voltage of SCs is the fabrication of asymmetric SCs (ASCs), wherein the positive electrode is of a faradaic or pseudocapacitive nature and the negative electrode is made of non-faradaic materials (Chodankar et al., 2017; Dubal et al., 2017). Generally, carbonaceous material is utilized as the negative electrode with oxide- or conducting polymer-based positive electrode to engineer ASCs. However, the low capacitance of carbon-based negative electrode limits the overall performance of ASCs, which fosters the requirement of an alternative for carbon-based negative electrode. Molybdenum nitride (MoN) can provide high capacitance due to pseudocapacitive behavior and is able to work in the negative potential window, which makes it a promising alternative to carbon-based negative electrode. Thus by coupling MoN negative electrode with another pseudocapacitive positive electrode, a high-performance ASC can be assembled (Liu et al., 2016; Shah et al., 2014). To provide proof of concept, we have selected ruthenium oxide (RuO_2) as the positive pseudocapacitive electrode because of its high capacitance and large overpotential for oxygen evolution in acidic electrolytes (Hu et al., 2006; Wang et al., 2014). So far, few reports are available on ASCs using RuO_2 and carbon as positive and negative electrodes, respectively (Shen et al., 2016; Choi et al., 2012).

In the present work, we have engineered a solid-state asymmetric pseudocapacitor using RuO_2 on carbon fabrics (RuO_2@CF) as the positive electrode and MoN nanoparticles coated on phosphorous-doped carbon fabrics (MoN@P-CF) as the negative electrode in 1 M H_2SO_4 electrolyte. Briefly, ultra-small MoN particles were uniformly decorated on P-doped carbon fabric (MoN@P-CF) using phosphomolybdic acid ($H_3PMo_{12}O_{40}$, PMo_{12}) as a single source of Mo and P, followed by ammonia annealing at the desired temperature. On the other hand, pseudocapacitive RuO_2 was grown on CF using a simple layer-by-layer (LBL) deposition method. Both the electrodes were initially tested in three-electrode configuration to evaluate their individual performances. The origin of improved electrochemical performances of MoN@P-CF in aqueous acidic electrolyte is unveiled by density functional theory (DFT) simulations.

RESULTS

Figure 1A shows the steps involved in the fabrication of all-pseudocapacitive solid-state ASCs along with synthesis methods used to develop phosphorus-doped carbon fabric cloth decorated with MoN nanocrystals (MoN@P-CF) and RuO_2 nanoparticles coated on flexible carbon fabric (RuO_2@CF). To prepare MoN@P-CF, initially PMo_{12} nanoclusters (phosphomolybdic acid, PMo_{12}) were anchored over the carbon fabric (CF) by the facile hydrothermal method, which will act as a single source of P and Mo. Later, PMo_{12}-coated CF (PMo_{12}@CF) undergoes heat treatment in ammonia (NH_3) atmosphere at a desired temperature to obtain MoN@P-CF. On the other hand, RuO_2 nanoparticles were directly grown over the CF using simple, low-cost, and scalable LBL method. Finally, using optimized MoN@P-CF as negative and RuO_2@CF as positive electrodes, all-pseudocapacitive solid-state asymmetric cell was assembled as shown in Figure 1A.

Design and Engineering of MoN@P-CF Negative Electrodes

The full-range X-ray photoelectron spectroscopic (XPS) spectrum of MoN@P-CF confirms the presence of carbon, molybdenum, nitrogen, and phosphorous. The core-level XPS spectra for C1s can be deconvoluted into four peaks as shown in Figure 1B. The peak observed at a binding energy (BE) of 284.8 eV can be assigned to graphitic carbon with C-C, whereas the other low-intensity peaks at 285.2, 285.8, and 286.2 eV may correspond to C bonding with phosphorous (C-P), nitrogen (C-N), and oxygen (C-O-C), respectively (Yan et al., 2015; Zhang et al., 2014a). The presence of C-P bond confirms the incorporation of P (from PMo_{12}) in carbon fabric. High-magnification XPS spectra of Mo3d exhibits a pair of Gaussian peaks at BEs of 228.8 and 232.2 eV (Figure 1C), which can be assigned to $Mo3d_{3/2}$ and $Mo3d_{5/2}$ of Mo-N bond (Yan et al., 2018). The N1s spectra shown in Figure 1D can be fitted in two major peaks where the peak at BE of 396.7 eV can be indexed to Mo-N bond from MoN, whereas the peak at 399.8 eV corresponds to the pyrrolic N (Zhang et al., 2014b). The high-resolution P2p spectrum shows a prominent peak at BE of 133.8 eV, which can be assigned to the boding between carbon and phosphorous, confirming the incorporation of P into CF (Figure 1E). The content of P in CF was determined to be 1.58 at %. Detailed analysis of samples unambiguously confirms the formation of P-doped CF coated with

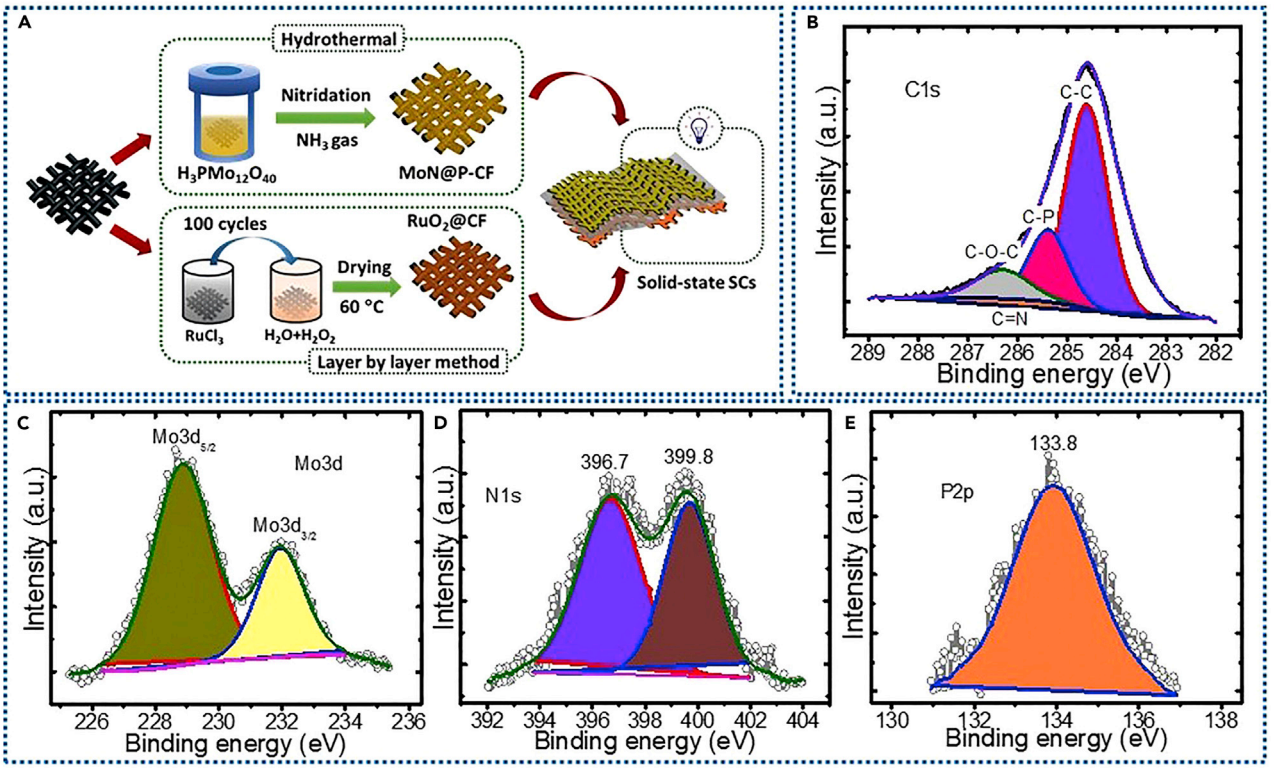

Figure 1. Schematic and XPS Analysis of MoN@P-CF

(A–E) (A) Schematic illustration of design and engineering of all-pseudocapacitive solid-state asymmetric supercapacitors. The steps involved in the synthesis of pseudocapacitive MoN@P-CF and RuO_2@CF are presented. XPS analysis of MoN@P-CF-900 sample: core-level XPS spectra with deconvoluted peaks (B) C1s, (C) Mo3d, (D) N1s, and (E) P2p.

MoN nanoparticles (MoN@P-CF). Thus we have provided a single-step method to accommodate adatom (P) in carbon structure and deposit ultra-small MoN nanoparticles on carbon fabric, which is expected to significantly improve the electrochemical performances. Figure 2A presents X-ray diffraction (XRD) patterns for the MoN@P-CF samples prepared at different nitridation temperatures. The XRD patterns exhibit six prominent diffraction peaks at 31.8°, 36.2°, 49.1°, 65.1°, 74.3°, 78.3°, which can be indexed to (002), (200), (202), (220), (222), and (204) planes, respectively, suggesting the formation of hexagonal MoN (JCPDS: 25–1367). The increase in peak intensity with nitridation temperature suggests the improved crystallinity of MoN nanocrystals. Thus the high nitridation temperature is favorable for complete conversion of PMo_{12} clusters into MoN nanocrystals. The inset of Figure 2A shows the typical hexagonal crystal structure of the MoN with layered configuration where the Mo atoms are sandwiched between the nitrogen atoms in the center of individual monolayers (Xie et al., 2014). To get further insights about the chemical bonding in MoN@P-CF, Raman analysis was performed and presented in Figure S1. Two major bands are observed at 1,350 cm^{-1} and 1,572 cm^{-1} (known as D and G band, respectively), which can be associated to the characteristic carbon peaks originating from carbon fabric (CF). The intensity ratio of D and G bands (I_D/I_G) presents the disorder degree of carbon materials. A small increase in the I_D/I_G ratio was found with temperature (0.94–0.99), which can be partly associated with the decoration of MoN nanocrystals and partly to the incorporation of phosphorous (P) in carbon framework during the nitridation process.

The scanning electron microscopic (SEM) analysis shows the uniform coating of MoN tiny nanoparticles on the surface of carbon fabric (Figure 2B). It is further observed that the size of MoN nanoparticles increases with annealing temperature (see Figure S1). The direct coating of MoN nanoparticles over the heteroatom-doped carbon fabric not only provides conducting scaffold but also avoids the use of unnecessary binders that will minimize the charge transfer resistance. The transmission electron microscopic (TEM) images revealed the formation of high-density ultra-small nanoparticles with sizes less than 10 nm (Figures 2C and

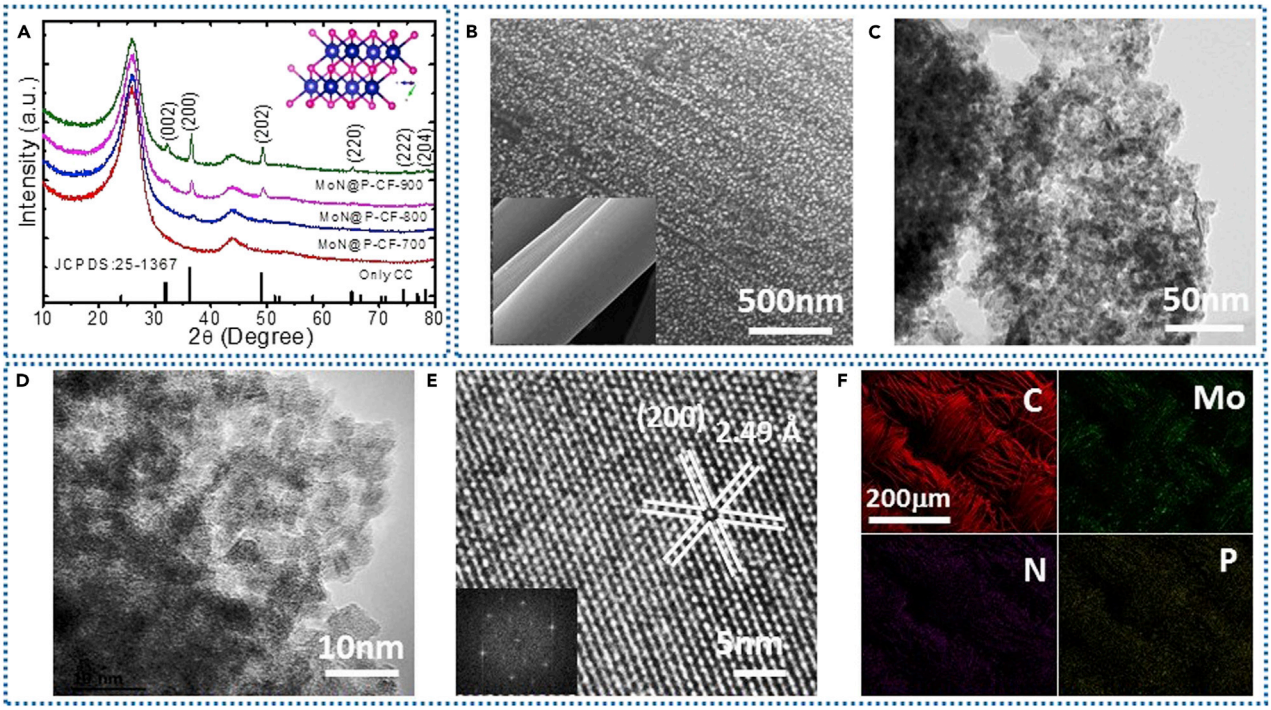

Figure 2. Characterizations of MoN@P-CF Samples

(A and B) (A) XRD patterns of MoN@P-CF samples prepared at different nitridation temperatures. Surface morphological analysis of MoN@P-CF-900 sample.
(B) SEM images of bare carbon fabric (inset) and P-doped carbon fabric with ultra-small MoN particles.
(C–E) (C and D) TEM images and (E) HRTEM image with corresponding fast Fourier transform spectrum.
(F) Large-area SEM-EDS mapping images, confirming the presence of C, Mo, N, and P.

2D). Such tiny nanoparticles provide highly accessible surface for the electrochemical reactions and short diffusion lengths for ionic transportation. To investigate the crystallinity of ultra-small MoN nanocrystals, high-resolution (HR) TEM images are recorded and shown in Figure 2E. An HRTEM image and fast Fourier transform reveals the lattice fringes with a d spacing of 2.4 Å, corresponding to the (200) plane of MoN. Moreover, the selected area electron diffraction (SAED) pattern confirms the polycrystalline nature of the as-prepared MoN nanocrystals (Figure S2). The different spots in the SAED pattern can be assigned to the hexagonal MoN structure. Energy-dispersive X-ray spectroscopic (EDX) analysis revealed the uniform distribution of the C, Mo, N, and P over the CF surface (Figure 2F). Thus it should be emphasized that the uniform coating of MoN nanodots in this hybrid material is a model for electrode or electrolyte surface polarization, as pseudocapacitive energy storage is based on surface redox processes. Indeed, this unique MoN@P-CF hybrid combines a heteroatom-doped (P) conducting porous CF with pseudocapacitive MoN nanocrystals, thus providing an optimal starting point from a structural point of view for high energy storage.

The electrochemical performances of MoN@P-CF electrodes were evaluated in standard three-electrode setup with 1 M H_2SO_4 electrolyte. The comparative cyclic voltammetry (CV) and charge/discharge curves (CD) curves for the MoN@P-CF electrodes prepared at different nitridation temperatures are shown in Figure S3. It is revealed that the sample prepared at 900°C (abbreviated as MoN@P-CF-900) shows higher integrated area under the CV curves with well-defined redox peaks, representing the best pseudocapacitive features. Moreover, the redox peaks can be retained at a high scanning rate of 100 mV/s, representing good rate capability of the prepared MoN@P-CF-900 electrode (Figure 3A). The charge storage mechanism of the as-prepared MoN@P-CF electrode was uncovered using the previous literature (Wang et al., 2007). Typically, the total charge storage in the electrode is the sum of surface capacitive (Q_s) and diffusion-controlled (Q_d) contributions. The capacitive contribution corresponds to the electrostatic adsorption of the electrolyte ions as well as surface redox reactions (pseudocapacitance), whereas diffusion-controlled contributions are associated with the surface and bulk electrochemical reactions. To quantify these

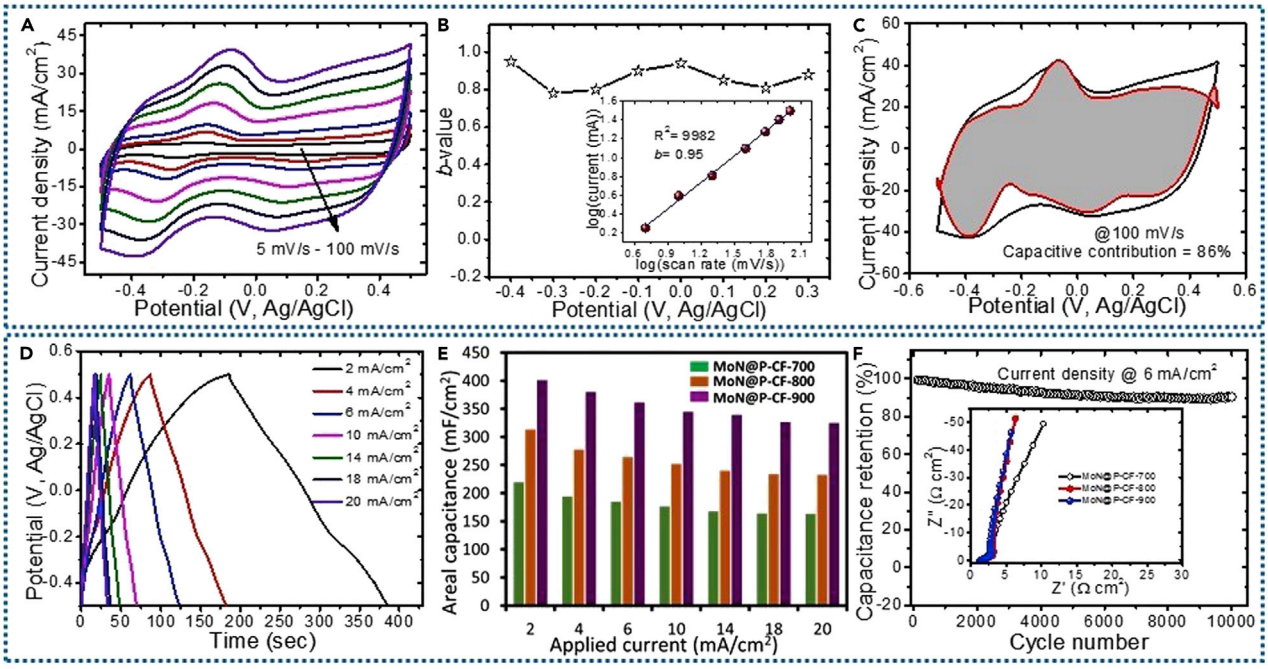

Figure 3. Electrochemical Characterizations of MoN@P-CF-900 with Three-Electrode Cell Design

(A) CV profiles recorded at different scanning rates in 1 M H_2SO_4 electrolyte.

(B) Variation of *b*-values with anodic potential scan. Inset shows power law dependence of peak current density at scan rates from 5–100 mV/s.

(C) Voltammetric response at a scan rate of 100 mV/s. The capacitive contribution to the total current is shown by the shaded region (86% of total charge contribution).

(D) Galvanostatic charge-discharge curves measured at different current densities from 2 to 20 mA/cm^2.

(E) Plot of areal capacitances as a function of current densities.

(F) Cycling stability was tested for 10,000 cycles at a current density of 6 mA/cm^2. Inset shows Nyquist plots for MoN@P-CF samples prepared at different nitridation temperatures.

contributions, the CV curves for MoN@P-CF-900 were recorded at different scan rates. By using the power law, it is possible to determine the charge storage mechanism of the electrode.

$$i = a \cdot v^b \qquad \text{(Equation 1)}$$

where "a" and "b" are adjustable parameters having defined conditions. Here, $b = 0.5$ suggests that the maximum current is contributed by diffusion-controlled processes, whereas $b = 1$ suggests purely capacitive processes. Using Equation 1, one can estimate the value of *b* by plotting the graph of log (i) versus log (v). Figure 3B shows the plot of *b*-values versus potentials, which lies between 0.8 and 0.95, suggesting the dominance of capacitive charge storage processes (Wang et al., 2007). The contribution from capacitive processes can be further quantified by assuming that the current response at the fixed potential is the combination of the capacitive (EDLC + pseudocapacitance) and diffusion-controlled processes as follows:

$$Q_t = Q_s + Q_d \qquad \text{(Equation 2)}$$

where Q_t is the total charge storage of the electrode. By considering the semi-infinite linear diffusion, it is possible to derive the Qs (capacitive contribution) by plotting total charge (Q_t) against the reciprocal of the square root of the scan rate ($v^{-1/2}$) according to the following equation:

$$Q_t = Q_s + kv^{-1/2} \qquad \text{(Equation 3)}$$

The surface capacitive and diffusion-controlled processes can be separated using Equation 3. Figure 3C shows the CV curves of calculated capacitive charges (shaded) and the experimental currents (solid line), suggesting that about 86% of the total current is contributed by capacitive storage at 100 mV/s. Thus the results demonstrate that the MoN@P-CF electrode is mainly pseudocapacitive in nature. The capacitive charge contribution increases with scan rates from 5 (56%) to 100 mV/s (86%) as shown in Figures S3 and S4, which can be explained by the fact that at a high scan rate the extrinsic surface effects due to both

pseudocapacitive charging and electronic conduction at the interface contribute to surface capacitive processes (Liu et al., 1998), whereas at slow scan rates, large currents originate from diffusion-controlled reactions in the acidic electrolyte, probably due to the higher mobility of protons (H^+). The high capacitive contribution at slow scan rates further suggests the good electrical conductivity of the electrode materials, which can be ascribed to P doping in CF and ultra-small MoN nanocrystals that offers super-highway and short diffusion for ion transportation.

To estimate the rate capability of as-prepared MoN@P-CF electrode, the galvanostatic CD measurements are carried out at different current densities (see Figure 3D). The linear CD curves without any potential drop even at high current density (20 mA/cm^2) display good capacitive features of the MoN@P-CF-900 electrode. In addition, the charging and discharging parts are perfectly symmetric to each other, implying highly reversible redox reactions. The areal capacitances were calculated from CD curves and plotted in Figure 3E. The MoN@P-CF-900 electrode delivers a maximum areal capacitance of 400 mF/cm^2 (598 F/g for mass loading of 1.4 mg/cm^2) at current density of 2 mA/cm^2, which decreases to 325 mF/cm^2 (505 F/g) at 20 mA/cm^2, retaining about 81% of initial capacitance. The MoN@P-CF900 electrode in the present investigation shows high gravimetric (areal) capacitance values (see Table S1), which can be attributed to good Ohmic contacts, ultra-small MoN nanocrystals, and P doping into CF. Nyquist plots for MoN@P-CF samples show linear dependency in the low-frequency region, indicating ideal capacitive behavior (inset of Figure 3F). Moreover, the low values of the equivalent series resistance (ESR) (1–1.2 Ω/cm^2) and charge transfer resistance in the high-frequency region imply good electrical conductivity with facile electrochemical interaction between the active material and electrolyte ions. Finally, the phase angles for MoN@P-CF electrodes in Bode plot (Figure S5) are close to 90°, signifying that MoN@P-CF sample shows an ideal capacitive performance. The cycling stability was recorded (Figure 3F) at a current density of 6 mA/cm^2, suggesting 91% capacitance retention over 10,000 cycles. The outperformance of MoN@P-CF can be credited to the uniform coating of ultra-small MoN nanocrystals on CF, which offer large electrochemically active sites and short diffusion paths for easy transportation of electrolyte ions. Moreover, the heteroatom (P)-doped carbon fabric matrix not only improves the electrical conductivity but also adds extra capacitive contribution in the charge storage.

To interpret the experimental results and link the atomic structure with the function of material, we have carried out DFT simulations. We have proposed following different models such as adsorption of H_3O^+ on CF, P-CF, MoN, and their nanocomposite interfaces (MoN@CF and MoN@P-CF), which are depicted in Figure S6. First, we discussed the adsorption energies of the doped systems and their interfaces by taking the adsorption energy on pristine CF as reference point (i.e., the adsorption energies of H_3O^+ are reported as the subtraction of adsorption energy on P-CF, MoN, MoN@CF, and MoN@P-CF from that on the pristine CF [ΔE_{ads}]). The simulations are performed for two atomic ratios (1 and 2), which generate six configurations by varying the number of bonds separating the two phosphorus atoms. In each configuration, multiple positions of H_3O^+ were optimized, and the best binder was selected for the discussion. The BE of H_3O^+ on CF and P-CF is negative, indicating that both pristine and P-doped CF systems have the ability to adsorb protons from the electrolyte solution. However, doping CF with one or two phosphorus atoms further enhances their adsorption capacity. The adsorption energies of P-CF and 2P-CF display much higher affinity toward H_3O^+ than pristine CF ($\Delta E_{ads=}$ −1.02 in case of P-CF and −1.44 eV in case of 2P-CF, see Table S2). In case of 2P-CF systems, H_3O^+ can be adsorbed on phosphorus or carbon atoms without significant preferences (note the difference between 2P1-CF and 2P32-CF). In 2P1-CF, H_3O^+ is adsorbed on phosphorus atom and both are out of the CF plane, whereas in 2P32-CF, H_3O^+ is adsorbed on carbon. To explain the trend of the adsorption energies and the nature of H_3O^+ bonding, bond charge density and Bader atomic charge analysis were performed. The bonding density is calculated as the difference between the density of the complex (H_3O^+@CF or P-CF) and density of the isolated fragments (CF or P-CF and H_3O^+). In case of CF and P-CF with 1 at % ratio, the insertion of n-type doping such as P enriches the electron density of the graphene fiber and induces polarized sites, which are beneficial for H_3O^+ binding (see Figure S7 and S8, and Table S3). The doping atom induces an electron transfer into the delocalized electron density over CF fiber because of electronegativity gradient between the P and C atoms (C: 2.55 and P: 2.19) (Figure S7).

It can be seen that an accumulated electron density on the adsorbed proton and the surrounding carbon atoms are higher in the doped fiber than in pristine. This indicates a charge transfer from H_3O^+ into CF and P-CF fibers where the bonding is ionic in nature. The gradient in electrostatic forces created between the

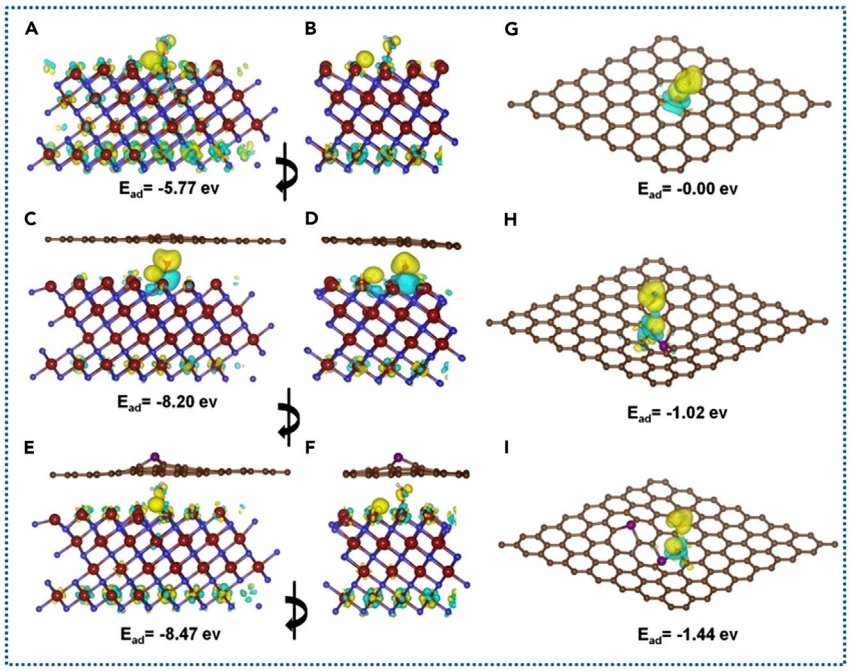

Figure 4. DFT Simulations of MoN@P-CF

(A–I) Bonding charge density (or charge density difference of H_3O^+ adsorption) on MoN (A and B), MoN@CF (C and D), MoN@P-CF (E and F), CF (G), P-CF (H), and 2P32-CF (I). (B, D, and F) are rotated views of (A, C, and D). Yellow and blue represent electron density rich and depletion. Isosurfaces are at a resolution of 0.015 electron/bhor^3; brown, dark blue, purple, plum, red, and white balls represent carbon, nitrogen, phosphorus, molybdenum, oxygen, and hydrogen atoms, respectively. H_3O^+ adsorption energies are reported in electron volts and are referenced to the adsorption on the pristine graphene (CF).

adsorbed proton and P or C (the adsorption site) increases the complex stability. As seen in Figure 4, P-CF-I and II display higher electron density accumulated on or around the adsorption site than that for pristine CF. The difference in the adsorption ability of P-CF I and II can be rationalized by the electrostatic repulsion between the negative charge on the adsorbed proton (H3) and the negative charges on the surrounding carbons atoms (C1, C5, and C13) with the lone pair on the oxygen atom (see Table S3). In contrast, in case of P-CF I system, these electrostatic forces are attractive, which enhances more the stability of the adsorbed proton. Adding more phosphorus atoms into CF fibers enriches the electron density and increases the polarization sites compared with the pristine CF or P-CF at 1 at % doping ratio (see Figure S7). The adsorption energies reported in Figure S9, and Table S2, indicate that the adsorption on P can be as high as on C atoms. However, the adsorption on the carbon atoms near the doping sites has higher ability to bind protons. Again, the balance between the electrostatic forces between the charges of the adsorbed protons and the substrate atoms at the adsorption site tunes the proton's affinity of the P-CF (see Figure S10 and Table S4).

Adsorption of H_3O^+ on MoN nanoparticles and their interfaces with CF and P-CF is modeled by calculating the adsorption energy on MoN slab of the hexagonal crystal and its interfaces with CF and P-CF (see Figure S6). The proton's affinity of these nanocomposites is getting much higher than that of pristine CF or P-CF. Results shown in Table S2 highlighted an important effect of molybdenum nitride as an interesting material for H_3O^+ adsorption, as well as its composites with CF and P-CF. The nanocomposite between MoN, CF, and P-CF improves further the proton's affinity. Moreover, P-CF proved to be a better stabilizing factor of the nanocomposite morphology than CF (see Figure S11). Indeed, the BE per unit area of MoN with CF and P-CF are −62.0 and −84.0 meV, respectively (importantly, this is the interaction energy between MoN-slab and CF and P-CF sheets). The optimized structures of H_3O^+ on top of the MoN slab and at its interfaces with MoN@CF and MoN@P-CF showed that H_3O^+ dissociates into H^+ and H_2O similar to the adsorption on CF and P-CF. The adsorbed proton localized between three MoN atoms, whereas H_2O molecules are directly coordinated to one (MoN@CF) or two Mo atoms (MoN@P-CF). Water adsorption

might help to stabilize the adsorbed proton by screening the electrostatic repulsion on the metal surface inversely to the CF and P-CF cases where H_2O molecules barely interact with the graphene atoms.

The binding charge density and atom in molecules (AIM) charges are presented in Figure 4 and Table S5. In case of H_3O^+@MoN complex, we observed that the surrounding Mo atoms are getting more positive and about 1.0 e is transferred into H_3O^+ (note charges on Mo114, Mo115, Mo118, and Mo122). The charge transfer from H_3O^+ is evidenced in binding charge density and atomic charges. The adsorbed proton undergoes a strong stabilizing interaction with positive charges on Mo atoms. This increases the polarization at adsorption site, which enhances the dipole-dipole, dipole-charge, and charge-charge interactions that are stabilizing adsorbed species (Figure 4). In case of MoN@CF and MoN@P-CF, more charge transfer from the metal surface into H_3O^+ (see Table S5) can be ascribed to the electron density flow coming from CF and P-CF into MoN surface. This strengthens the dipole moment created at adsorption site, which stabilizes further the adsorbed protons. The slight difference between P-CF and CF is due to the presence of positive charge at the phosphorus atom (+1.68e) that decreases the electrostatic repulsion between the adsorbed protons and the electron cloud delocalized over the graphene fiber (Figures 4 and S11).

Altogether, our DFT simulations enabled us to get deeper atomic insights into the n-type doping effect, which enhances the proton adsorption as well as the thermodynamic stability of the nanocomposite formed between the MoN nanoparticles and P-CF. Also, our results emphasize on the high affinity of proton of MoN nanoparticles, which is beneficial for the energy storage industry.

Fabrication of RuO_2@CF Positive Electrode

RuO_2 nanoparticles were directly grown on carbon fabrics, for the first time using simple and scalable LBL method. The deposition kinetics of RuO_2 nanoparticles is based on ion-by-ion growth mechanism, which involves the deposition of Ru species at the CF surface and then reaction with O species forming a nucleation center (RuO_2 monolayer). XRD pattern for RuO_2@CF shows two prominent peaks at 26.5° and 43.5° that are assigned to the carbon fabric (Figure S12). There is no peak found for RuO_2 nanoparticles, suggesting the formation of amorphous phase. It is reported that the amorphous RuO_2 shows better capacitive features than the crystalline one due to easy access to protons or ions for electrochemical reactions, and therefore whole electrode material can be utilized for the charge storage process (Dubal et al., 2013). The highly magnified XPS spectra for Ru3p of RuO_2@CF sample shown in Figure 5A can be split into two peaks at BEs of 484.6 and 462.4 eV, suggesting the formation of RuO_2 (Dubal et al., 2013; Hu et al., 2006). Moreover, the core-level XPS spectra for the O1s (Figure 5B) can be fitted into three major peaks at BEs of 529.7, 531.2, and 532.6 eV, which are ascribed to the metal (Ru)-oxygen bond, metal-OH bond, and the H-O-H bonding in residual water, respectively (Hu et al., 2006). It is further realized that the surface of the RuO_2 is hydroxylated to form surface oxyhydroxide, which might increase surface wettability and improve the interactions between electrode material and electrolyte. Surface morphological analysis shows homogeneous distribution of RuO_2 nanoparticles over the entire exposed surface of the CF. The single carbon fabric densely coated with RuO_2 nanoparticles can be observed in Figure 5C. The highly magnified SEM image (Figure 5D) further confirms the formation of fractal-like agglomerates of fine RuO_2 nanoparticles, leaving ample free space between them, facilitating ion transport processes. To get more insights about the nanostructure of RuO_2, TEM analysis was carried out and shown in Figure 5E, which shows the formation of tiny nanoparticles with size in the range of 5–10 nm. These tiny RuO_2 nanoparticles directly grown on carbon fabric can offer short ion-transport pathways and favor the direct contact of electrolytes to the interfacial electrochemically active species, consequently enhancing the supercapacitive performance. The uniform distribution of Ru and O on the carbon fabric (CF) can be further evidenced by EDX analysis, as shown in Figure S12.

The electrochemical properties of the as-prepared RuO_2@CF was investigated using three-electrode cell in 1 M H_2SO_4 electrolyte. The CV curves for RuO_2@CF recorded at different scan rates exhibits semi-rectangular shapes over a wide potential range of 0–1 V (versus Ag/AgCl) (see Figure S12). The shapes of CV curves can be retained even at a high scan rate of 100 mV/s, indicating highly reversible redox transitions of RuO_2@CF electrode, which meets the high-power requirement of SCs. These worthy electrochemical properties might be attributed to the amorphous and tiny nanoparticulate structure of hydrous RuO_2@CF that offers facile transport pathways for both protons and electrons. The energy storage or delivery process within hydrous RuO_2 generally obeys the following equation:

$$RuO_2 + dH^+ + de^- \leftrightarrow RuO_{2-d}(OH)_d \quad (0<d<2) \qquad \text{(Equation 4)}$$

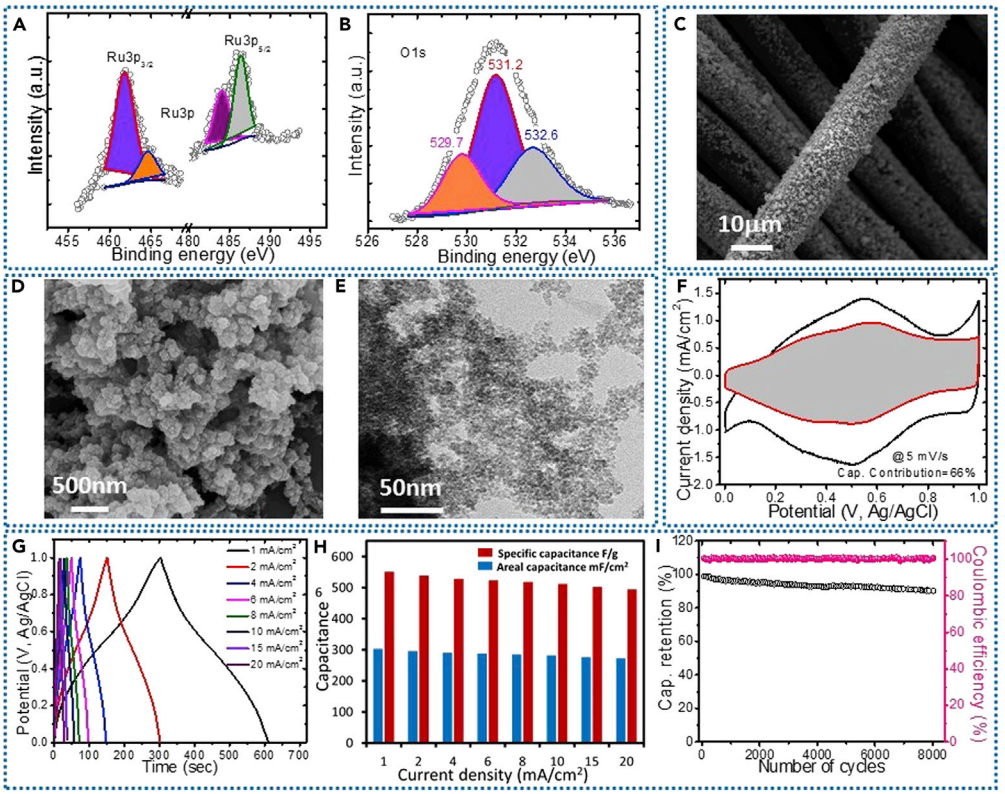

Figure 5. Physicochemical and Electrochemical Characterizations of RuO_2@CF

(A and B) Magnified XPS spectra for Ru3p and O1s, respectively.

(C–F) (C and D) SEM images of RuO_2 coated on carbon fabrics, (E) TEM image, showing uniform distribution of tiny nanoparticles without any aggregation. Electrochemical performance evaluation of RuO_2@CF in three-electrode configuration: (F) CV curves at scan rate of 5 mV/s. The shaded area represents the capacitive contribution to the total current.

(G) Galvanostatic charge-discharge profiles at different current densities.

(H) Variation of areal and specific capacitances with current densities.

(I) Long-term cycling test with corresponding Coulombic efficiency measured at 10 mA/cm^2 over 8,000 cycles.

To provide evidence of the pseudocapacitive nature of RuO_2@CF, *b*-value was calculated using Equation 1, which was found to be 0.92 as shown in Figure S13. It can be further seen from Figure 5F that about 66% of the total current of RuO_2@CF electrode is contributed by the capacitive mechanism at 5 mV/s. The capacitive charge contribution increases with scan rates from 5 to 100 mV/s, reaching 93% at 100 mV/s as shown in Figure S14. The galvanostatic charge/discharge (GCD) measurements for RuO_2@CF electrode were performed at different current densities within the potential range of 0–1 V (versus Ag/AgCl), as shown in Figure 5G. All charge curves are symmetric to their discharging counterparts, implying fast and reversible electrochemical features. The maximum areal capacitance for RuO_2@CF electrode was found to be 303 mF/cm^2 (551 F/g) at a current density of 1 mA/cm^2, which was decreased to 272 mF/cm^2 (494 F/g) at 20 mA/cm^2, retaining about 88% of initial capacitance (Figure 5H). The cycling performance was tested at a current density of 10 mA/cm^2 over 8,000 cycles. As can be seen from Figure 5I, the RuO_2@CF electrode exhibited good cycling stability of 87% retention of initial capacitance after 8,000 cycles. Moreover, RuO_2@CF electrode shows good Coulombic efficiency (almost 100%) over 8,000 cycles, which is beneficial for the high-power applications. The decrease in capacitance by a small amount with cycles can be ascribed to the loss of active material caused by the dissolution or detachment, during the early charging or discharging cycles in the electrolyte. The overall resistance contributions including ESR, charge transfer resistance, and current collectors was determined to be 2.2 Ω, as seen from the inset of Figure S13. Moreover, the relaxation time constant was determined to be τ_0 = 22 ms, suggesting fast response of the RuO_2@CF electrode.

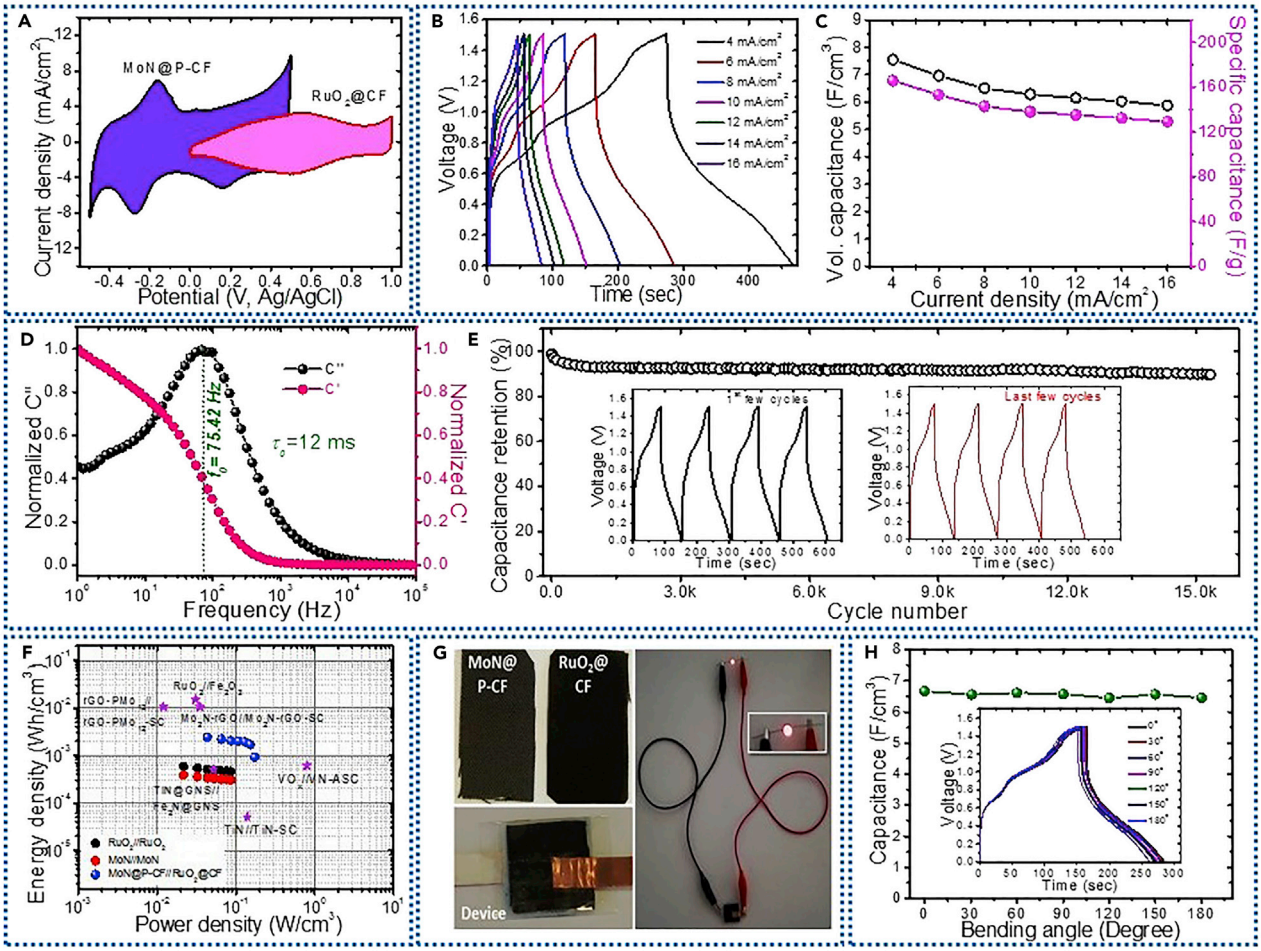

Figure 6. Electrochemical Testing of All-Pseudocapacitive Solid-State Asymmetric Cell, MoN@P-CF//RuO_2@CF

(A) CV curves for the MoN@P-CF and RuO_2@CF electrodes at constant scan rate of 10 mV/s in different working voltage windows.

(B) CD profiles recorded at different current densities.

(C) Variation of specific and volumetric capacitances with the current density.

(D) Plot of real and imaginary capacitances as a function of frequency.

(E) The plot of capacitance retention with cycle number over 15,000 cycles measured at 12 mA/cm^2; inset shows the first and last charge-discharge cycles.

(F) Ragone plot with comparison of energy and power density values with the literature.

(G) Practical demonstration of MoN@P-CF//RuO_2@CF cell by powering a red light-emitting diode during the discharge state.

(H) The graph of variation of capacitance with bending angle of device; inset shows CD curves of asymmetric cell at different bending angles.

All-Pseudocapacitive Solid-State Asymmetric Supercapacitor (MoN@P-CF//RuO_2@CF)

To demonstrate the commercial feasibility of MoN@P-CF hybrid electrode, all-pseudocapacitive asymmetric solid-state SC was assembled using MoN@P-CF and RuO_2@CF as negative and positive electrodes, respectively, with PVA-H_2SO_4 gel electrolyte. It is important to note that to achieve the highest cell voltage, the charges stored in both electrodes must be balanced, which can be done by adjusting the mass loading in each electrode. The calculated mass ratio from MoN to RuO_2 electrode is 1:2 (see Methods section) with a total mass loading of 3.4 mg/cm^2. The CV curves for MoN@P-CF and RuO_2@CF electrodes suggest that both electrodes can work in different potential windows, proposing the cell voltage of 1.5 V for MoN@P-CF//RuO_2@CF cell (Figure 6A). The CV curves recorded at different scan rates (see Figure S15) show a prominent redox pair, confirming the dominance of Faradaic charge storage mechanism. These redox peaks can be retained at high scan rates of 100 mV/s, implying good reversibility of the electrode materials in device. The CD profiles of MoN@P-CF//RuO_2@CF asymmetric cell show non-linear shapes as observed in CV results, which can be assigned to the pseudocapacitive nature of electrodes (Figure 6B). The cell delivers a maximum capacitance of 7.54 F/cm^3 at a current

density of 4 mA/cm^2, which can be retained to 5.88 F/cm^3 when the current density was increased to 16 mA/cm^2 (78% retention), as shown in Figure 6C. The good rate capability of the cell can be attributed to the fact that all the active sites of electrode materials are easily reachable for the electrolyte ions even at high current density. In addition, the rapid redox reactions, kinetic balance, and capacity matching of both electrodes can also be responsible for high capacitance and good rate performance. The obtained capacitance for MoN@P-CF//RuO_2@CF cell is the highest value reported so far; for example, MnO_2// WON (tungsten oxynitride) (2.73 F/cm^3) (Yu et al., 2015), rGO-PW_{12}//rGO-PMo_{12} (3.91 F/cm^3) (Dubal et al., 2017), Fe_2O_3//MnO_2 (1.2 F/cm^3) (Lu et al., 2014).

The high rate performance of MoN@P-CF//PPy@CF asymmetric cell was studied by electrochemical impedance analysis within the frequency range of 100 kHz to 1 Hz with an amplitude of 5 mV. Nyquist plot for the asymmetric cell shows an ESR of only 1.2 Ω/cm^2, manifesting good electrical conductivity of both the electrode materials as well as strong binding between the active electrode material and current collector (Figure S15). The low charge transfer resistance (small semicircle) can be attributed to the good interaction between electrode material and electrolyte. In the low-frequency region, our device exhibits typical capacitive behavior, where a vertical line nearly parallel to the y axis is observed. The capacitive characteristics was further approved by the Bode plot where a phase is close to 90° (Figure S15). The real (C′) and imaginary capacitances (C″) at different frequencies for MoN@P-CF//PPy@CF cell are calculated and shown in Figure 6D. The plot shows common relaxation-type dispersions where the real capacitance C′ decreases with frequency, whereas C″ shows a maximum. The relaxation time constant (τ_0) is the minimum time needed to discharge all the energy with efficiency greater than 50% and can be calculated using $\tau_0 = 1/f_0$ (where f_0 is characteristic frequency). The τ_0 for MoN@P-CF//RuO_2@CF device was calculated to be 12 ms (for the corresponding frequency of 82.87 Hz and 13 ms from Bode plot at 11.5 Hz) as displayed in Figure 6D. Such a small relaxation time (τ_0) signifies that this all-pseudocapacitive asymmetric cell exhibits ultra-fast power output. This small τ_0 value for the MoN@P-CF//RuO_2@CF cell is promising than the values reported for fast-charging SCs in the literature: RuO_2//$Ti_3C_2T_x$ asymmetric cell (740 ms) (Jiang et al., 2018) and symmetric cells based on titanium nitride (TiN, 12.5–25 ms) (Yu et al., 2015), carbon anions (26 ms) (Pech et al., 2010), and laser-scribed graphene (19 ms) (El-Kady and Kaner, 2013). The extremely small relaxation time constant further confirms the ultra-fast charge-discharge ability of our asymmetric cell, which makes it promising for advanced portable electronic devices. The cycling stability for our asymmetric cell was performed at constant current density of 12 mA/cm^2 over 15,000 cycles as shown in Figure 6E. The device exhibited a capacitance retention of 89% over 15,000 cycles. The energy and power densities define the real-world applications of energy storage devices. From CD curves, we have estimated the energy and power densities of MoN@P-CF//RuO_2@CF cell and compared with the literature values. The cell delivers energy density of 2.36 mWh/cm^3 (at power density of 43 mW/cm^3), which is comparable with that of carbon-based micro-SCs and lithium thin-film batteries (10^{-3} -10^{-2} Wh/cm^3) and is significantly higher than those of previously reported flexible metal nitride SCs (0.05 mWh/cm^3) (Lu et al., 2012). Even at a high power density of 174 mW/cm^3 our MoN@P-CF//RuO_2@CF device maintains an energy density of 1.8 mWh/cm^3, confirming the capacity of device to provide high energy and high power in one system (Figure 6F). The summary of comparison of literature values is provided in Table S6 and Figure S15 (Lu et al., 2012, 2013; Jiang et al., 2018; Zhu et al., 2015; Ma et al., 2015; Tan et al., 2018), for example, VOx//VN (0.61 mW/cm^3) (Lu et al., 2013), TiN@GNS//Fe_2N@GNS (0.51 mW/cm^3) (Zhu et al., 2015), and TiN//TiN (0.05 mW/cm^3) (Lu et al., 2012). The energy efficiency (E_{eff}) of the asymmetric cell was determined to be 73.2% at 4 mA/cm^2 and 81.1% at 12 mA/cm^2 with an average value of above 70%, which is slightly poor than the previous reports (Javed et al., 2018) as shown in Figure S15. The practical applicability of cell is presented using a demonstration with red light-emitting diodes as shown in Figure 6G. The bending test was further executed consecutively, and angles were altered manually, as indicated in Figure 6H. The corresponding CD curves recorded at different bending angles are shown in the inset of Figure 6H. The negligible change in capacitance and shapes of the CD curves even at bending angle of 180° assures its good flexibility and mechanical stability. These good electrochemical features can be credited to interactive contributions of both electrode materials and the all-pseudocapacitive asymmetric cell design, which are summarized as follows. (1) Binderless nanostructured electrode materials avoid unnecessary binders and minimize the ESR. Moreover, heteroatom (phosphorus) doping in CF provides additional pseudocapacitance. (2) Tiny nanoparticles of MoN and RuO_2 electrodes provide easy access to electrochemical sites and short diffusion paths for ionic transportation. (3) The complementary potential windows of the RuO_2 and MoN electrodes in H_2SO_4 electrolyte allow to develop new high-voltage all-pseudocapacitive asymmetric cell with improved energy density.

DISCUSSION

In summary, we have designed and engineered ultra-fast all-pseudocapacitive solid-state ASC by coupling ultra-small MoN particles coated on P-doped CF (MoN@P-CF) negative electrode with RuO_2@CF positive electrode. Our DFT simulations showed that the adsorption is further enhanced on MoN surface as well as at its interfaces with P-CF, which will provide guidelines to develop nitride-based pseudocapacitors. Owing to the excellent pseudocapacitive properties of both electrodes, MoN@P-CF//RuO_2@CF asymmetric cell delivered a high capacitance (7.74 F/cm^3), high energy (2.4 mWh/cm^3), and power densities (174 mW/cm^3) with good cycling stability (89%) over 15,000 cycles. Moreover, the device demonstrated extremely small relaxation time (τ_0) of 12 ms, significantly lower than that for conventional carbon-based (EDLC) SCs, which can be directly applied in high-power microelectronics and in many diverse flexible and wearable electronics.

Limitations of the Study

For currently used polyoxometalates (POM) precursor, it is difficult to alter the nanoparticulate morphology of MoN and control the concentration of P-doping in CF, which limits further enhancement of its electrochemical performances. It is anticipated that by employing other suitable precursors, the nanostructure of MoN and the amount of P-doping can be further optimized, achieving higher performance of the asymmetric pseudocapacitors.

METHODS

All methods can be found in the accompanying Transparent Methods supplemental file.

SUPPLEMENTAL INFORMATION

Supplemental Information can be found online at https://doi.org/10.1016/j.isci.2019.05.018.

ACKNOWLEDGMENTS

D.P.D. acknowledges Queensland University of Technology and Australian Research Council (ARC) for the Future Fellowship (FT180100058). S.A.-A. acknowledges the computational resource of the college of Engineering and Geosciences (CPG) (Alfahd supercomputer) employed for the DFT simulations.

AUTHOR CONTRIBUTIONS

D.P.D. and Y.-K.H. designed the experiments, analyzed the data, and wrote the manuscript. D.P.D. carried out synthesis and characterization of electrode materials. S.A.-A. performed all the DFT calculations and interpreted the results. D.P.D. and N.R.C. designed and carried out electrochemical measurements of electrodes and devices. All authors contributed equally to the preparation and reviewing manuscript.

DECLARATION OF INTERESTS

The authors declares no competing interest.

Received: March 25, 2019
Revised: May 2, 2019
Accepted: May 11, 2019
Published: June 28, 2019

REFERENCES

Augustyn, V., Simon, P., and Dunn, B. (2014). Pseudocapacitive oxide materials for high-rate electrochemical energy storage. Energy Environ. Sci. *7*, 1597–1614.

Balogun, M.S., Qiu, W., Wang, W., Fang, P., Lu, X., and Tong, Y. (2015). Recent advances in metal nitrides as high-performance electrode materials for energy storage devices. J. Mater. Chem. A *3*, 1364–1387.

Balogun, M.S., Huang, Y., Qiu, W., Yang, H., Ji, H., and Tong, Y. (2017). Updates on the development of nanostructured transition metal nitrides for electrochemical energy storage and water splitting. Mater. Today *20*, 425–451.

Borenstein, A., Hanna, O., Attias, R., Luski, S., Brousse, T., and Aurbach, D. (2017). Carbon-based composite materials for supercapacitor electrodes: a review. J. Mater. Chem. A *5*, 12653–12672.

Choi, B.G., Chang, S., Kang, H., Park, C., Kim, H., Hong, W., Lee, S., and Huh, Y. (2012). High performance of a solid-state flexible asymmetric supercapacitor based on graphene films. Nanoscale *4*, 4983–4988.

Chodankar, N.R., Dubal, D.P., Kwon, Y., and Kim, D.H. (2017). Direct growth of $FeCo_2O_4$ nanowire arrays on flexible stainless steel mesh for high-performance asymmetric supercapacitor. NPG Asia Mater. *9*, e419.

Dubal, D.P., Gund, G.S., Holze, R., Jadhav, H.S., Lokhande, C.D., and Park, C. (2013). Solution-based binder-free synthetic approach of RuO_2 thin films for all solid state supercapacitors. Electrochim. Acta *103*, 103–109.

Dubal, D.P., Ayyad, O., Ruiz, V., and Gomez-Romero, P. (2015). Hybrid energy storage: the merging of battery and supercapacitor chemistries. Chem. Soc. Rev. *44*, 1777–1790.

Dubal, D.P., Chodankar, N.R., Vinu, A., Kim, D.H., and Gomez-Romero, P. (2017). Asymmetric supercapacitors based on reduced graphene oxide with different polyoxometalates as positive and negative electrodes. ChemSusChem *10*, 2742–2750.

Dubal, D.P., Chodankar, N.R., Kim, D.H., and Gomez-Romero, P. (2018). Towards flexible solid-state supercapacitors for smart and wearable electronics. Chem. Soc. Rev. *47*, 2065–2129.

El-Kady, M.F., and Kaner, R.B. (2013). Scalable fabrication of high-power graphene micro-supercapacitors for flexible and on-chip energy storage. Nat. Commun. *4*, 1475.

Eftekhari, A., and Mohamedi, M. (2015). Tailoring pseudocapacitive materials from a mechanistic perspective. Mater. Today *18*, 252–264.

Hu, C.C., Chang, K.H., Lin, M.C., and Wu, Y.T. (2006). Design and tailoring of the nanotubular arrayed architecture of hydrous RuO_2 for next generation supercapacitors. Nano Lett. *6*, 2690–2695.

Javed, M.S., Shah, H.U., Shaheen, N., Lin, R., Qiu, M., Xie, J., Li, J., Raz, R., Mai, W., and Hu, C. (2018). High energy density hybrid supercapacitor based on 3D mesoporous cuboidal Mn_2O_3 and MOF-derived porous carbon polyhedrons. Electrochim. Acta *282*, 1–9.

Jiang, Q., Kurra, N., Alhabeb, M., Gogotsi, Y., and Alshareef, H.N. (2018). All pseudocapacitive MXene-RuO_2 asymmetric supercapacitors. Adv. Energy Mater. *8*, 1703043.

Ko, Y., Kwon, M., Bae, W., Lee, B., Lee, S., and Cho, J. (2017). Flexible supercapacitor electrodes based on real metal-like cellulose papers. Nat. Commun. *8*, 536.

Liu, T.C., Pell, W.G., Conway, B.E., and Roberson, S.L. (1998). Behavior of molybdenum nitrides as materials for electrochemical capacitors comparison with ruthenium oxide. J. Electrochem. Soc. *145*, 1882–1888.

Liu, J., Huang, K., Tang, H.L., and Lei, M. (2016). Porous and single-crystalline-like molybdenum nitride nanobelts as a non-noble electrocatalyst for alkaline fuel cells and electrode materials for supercapacitors. Int. J. Hydrogen Energy *41*, 996–1001.

Lu, X., Wang, G., Zhai, T., Yu, M., Xie, S., Ling, Y., Liang, C., Tong, Y., and Li, Y. (2012). Stabilized TiN nanowire arrays for high-performance and flexible supercapacitors. Nano Lett. *12*, 5376–5381.

Lu, X., Zeng, Y., Yu, M., Zhai, T., Liang, C., Xie, S., Balogun, M., and Tong, Y. (2014). Oxygen-deficient hematite nanorods as high-performance and novel negative electrodes for flexible asymmetric supercapacitors. Adv. Mater. *26*, 3148–3155.

Lu, X., Yu, M., Zhai, T., Wang, G., Xie, X., Liu, T., Liang, C., Tong, Y., and Li, Y. (2013). High energy density asymmetric quasi-solid-state supercapacitor based on porous vanadium nitride nanowire anode. Nano Lett. *13*, 2628–2633.

Ma, G., Wang, Z., Gao, B., Ding, T., Zhong, Q., Peng, X., Su, J., Hu, B., Yuan, L., Chu, P., et al. (2015). Multilayered paper-like electrodes composed of alternating stacked mesoporous Mo_2N nanobelts and reduced graphene oxide for flexible all-solid-state supercapacitors. J. Mater. Chem. A *3*, 14617–14624.

Nam, K., Kim, D., Yoo, P., Chiang, C., Meethong, N., Hammond, P., Chiang, Y., and Belcher, A. (2006). Virus-enabled synthesis and assembly of nanowires for lithium ion battery electrodes. Science *312*, 885–888.

Nitta, N., Wu, F., Lee, J.T., and Yushin, G. (2015). Li-ion battery materials: present and future. Mater. Today *18*, 252–264.

Pech, D., Brunet, M., Durou, H., Huang, P., Mochalin, V., Gogotsi, Y., Taberna, P., and Simon, P. (2010). Ultrahigh-power micrometre-sized supercapacitors based on onion-like carbon. Nat. Nanotechnol. *5*, 651–654.

Shah, S.I.U., Hector, A.L., and Owen, J.R. (2014). Redox supercapacitor performance of nanocrystalline molybdenum nitrides obtained by ammonolysis of chloride- and amide-derived precursors. J. Power Sources *266*, 456–463.

Salanne, M., Rotenberg, B., Naoi, K., Kaneko, K., Taberna, P., Grey, C., Dunn, B., and Simon, P. (2016). Efficient storage mechanisms for building better supercapacitors. Nat. Energy *1*, 16070.

Shen, B., Zhang, X., Guo, R., Lang, J., Chen, J., and Yan, X. (2016). Carbon encapsulated RuO_2 nano-dots anchoring on graphene as an electrode for asymmetric supercapacitors with ultralong cycle life in an ionic liquid electrolyte. J. Mater. Chem. A *4*, 8180–8189.

Tan, Y., Meng, L., Wang, Y., Dong, W., Kong, L., Kang, L., and Ran, F. (2018). Negative electrode materials of molybdenum nitride/N-doped carbon nano-fiber via electrospinning method for high-performance supercapacitors. Electrochim. Acta *277*, 41–49.

Wang, G., Zhang, L., and Zhang, J. (2012). A review of electrode materials for electrochemical supercapacitors. Chem. Soc. Rev. *41*, 797–828.

Wang, W., Guo, S., Lee, I., Ahmed, K., Zhong, J., Favors, Z., Zaera, F., Ozkan, M., and Ozkan, C. (2014). Hydrous ruthenium oxide nanoparticles anchored to graphene and carbon nanotube hybrid foam for supercapacitors. Sci. Rep. *4*, 4452.

Wang, J., Polleux, J., Lim, J., and Dunn, B. (2007). Pseudocapacitive contributions to electrochemical energy storage in TiO_2 (Anatase) nanoparticles. J. Phys. Chem. C *111*, 14925–14931.

Xie, J., Li, S., Zhang, X., Zhang, J., Wang, R., Zhang, H., Pan, B., and Xie, Y. (2014). Atomically-thin molybdenum nitride nanosheets exposing active surface sites for efficient hydrogen evolution. Chem. Sci. *5*, 4615–4620.

Yan, H., Tian, C., Wang, L., Wu, A., Meng, M., Zhao, L., and Fu, H. (2015). Phosphorus-modified tungsten nitride/reduced graphene oxide as a high-performance, non-noble-metal electrocatalyst for the hydrogen evolution reaction. Angew. Chem. Int. Ed. *54*, 6325–6329.

Yan, H., Jiao, Y., Wu, A., Tian, C., Wang, L., Zhang, X., and Fu, H. (2018). Synergism of molybdenum nitride and palladium for high-efficient formic acid electrooxidation. J. Mater. Chem. A *6*, 7623–7630.

Yang, P., Chao, D., Zhu, C., Xia, X., Zhang, Y., Wang, X., Sun, P., Tay, B., Shen, Z., Mai, W., and Fan, H. (2016). Ultrafast-charging supercapacitors based on corn-like titanium nitride nanostructures. Adv. Sci. *3*, 1500299.

Yuan, Y., Amine, K., Lu, J., and Shahbazian-Yassar, R. (2017). Understanding materials challenges for rechargeable ion batteries with in situ transmission electron microscopy. Nat. Commun. *8*, 15806.

Yu, M., Han, Y., Cheng, X., Hu, L., Zeng, Y., Chen, M., Cheng, F., Lu, X., and Tong, Y. (2015). Holey tungsten oxynitride nanowires: novel anodes efficiently integrate microbial chemical energy conversion and electrochemical energy storage. Adv. Mater. *15*, 3085–3091.

Yu, X.Y., and Lou, X.W. (2018). Mixed metal sulfides for electrochemical energy storage and conversion. Adv. Energy Mater. *8*, 1701592.

Zhang, B., Cui, G., Zhang, K., Zhang, L., Han, P., and Dong, S. (2014a). Molybdenum nitride/nitrogen-doped graphene hybrid material for lithium storage in lithium ion batteries. Electrochim. Acta *150*, 15–22.

Zhang, W., Wu, Z.Y., Jiang, H.L., and Yu, S.H. (2014b). Nanowire-directed templating synthesis of metal–organic framework nanofibers and their derived porous doped carbon nanofibers for enhanced electrocatalysis. J. Am. Chem. Soc. *136*, 14385–14388.

Zhu, C., Yang, P., Chao, D., Wang, X., Zhang, X., Chen, S., Tay, B., Huang, H., Zhang, H., Mai, W., and Fan, H. (2015). All metal nitrides solid-state asymmetric supercapacitors. Adv. Mater. *27*, 4566–4571.

ISCI, Volume *16*

Supplemental Information

Molybdenum Nitride Nanocrystals Anchored on Phosphorus-Incorporated Carbon Fabric as a Negative Electrode for High-Performance Asymmetric Pseudocapacitor

Deepak P. Dubal, Safwat Abdel-Azeim, Nilesh R. Chodankar, and Young-Kyu Han

Transparent Methods

Chemicals

The phosphomolybdic acid ($H_3PMo_{12}O_{40}.3H_2O$ Kegging type, PMo_{12}), hydrochloric acid (HCl), acetone (C_3H_6O), ethanol (C_2H_6O), hydrogen peroxide (H_2O_2) and Ruthenium (III) chloride ($RuCl_3 \cdot xH_2O$), polyvinyl alcohol (PVA) was purchased from sigma Aldrich. The carbon fabric (W0S1002 Carbon Cloth Substrate with thickness 360 μm) was purchased from FC Internationals, South Korea. All regents were used as received without further purification. All the precursor solutions were prepared by using the MilliQ water.

Design and synthesis of MoN@P-CF

Prior to the deposition, the commercial CF was cleaned with acetone, ethanol and deionized (DI) water using ultrasonic bath (20 min each) and dried in the oven at temperature 80 °C for 24 hr. Initially, well-cleaned CF was immersed in 10 mM phosphomolybdic acid ($H_3PMo_{12}O_{40}.3H_2O$, PMo_{12}) solution and sonicated for 30 min. Later, the precursor solution with CF was transferred to Teflon-linked stainless steel autoclave and treated at 120°C for 12 h to achieve PMo_{12} nanoclusters decorated CF. The PMo_{12}@CF sample was cleaned with MilliQ water and dried in vacuum oven at 70 °C for 12 hr. Finally, the as-prepared PMo_{12}@CF were annealed in tube furnace under ammonia gas flow with a temperature rate of 3 ^oC/min at three different temperatures 700 °C, 800 °C and 900 °C for 5 hours. The prepared samples were denoted as MoN@P-CF-700, MoN@P-CF-800 and MoN@P-CF-900. All the samples were preserved in vacuum sealed desiccator to avoid the oxidation.

Synthesis of RuO_2 on carbon fabric (CF)

This is the first report on the synthesis of RuO_2 on CF by Layer-by-Layer (LBL) deposition method. This is very simple, cost-effective and large scale deposition method. For the deposition of RuO_2 on CF, 10 mM $RuCl_3$ was used as the cationic precursor while MilliQ water with 3-4 drops of H_2O_2 maintained at 80 °C was utilized as anionic precursor solution. Pre-cleaned CF substrate was immersed in a cationic solution ($RuCl_3$) for 20 sec where the ruthenium species adsorbed on to the CF surface. The CF-substrate was rinsed in MilliQ water for 5 sec to remove loosely bound Ru species. Later, Ru-species@CF substrate was immersed in anionic solution (kept at 80 °C) for 20 sec to form a layer of hydrous ruthenium oxide material. Finally, the CF-substrate was again rinsed for 5 sec to remove excess or unreacted species. We have performed 120 deposition cycles to get a terminal thickness where the mass loading was determined to be 0.9 mg/cm^2. After complete reaction cycles, the RuO_2@CF samples were cleaned with water and dried in vacuum oven for 12 hr at 70 °C.

Materials characterizations

All the samples were characterized by using different characterizations techniques. The structural analysis was performed by Powder X-ray diffraction patterns using X-ray Powder Diffractometer (Rigaku MiniFlex600) (Cu Kα radiation and PIXel detector). The compositional information as collected using Raman spectra, which was recorded using Raman Spectrometer (Horiba Scientific). The oxidation states and surface composition various elements in the sample was measured using X-ray photoelectron spectroscopy XPS (ESCALAB-MKII). The surface morphological analysis were performed using series of characterization techniques such as field-emission scanning electron microscopy, FE-SEM (FEI Quanta 450 FEG Environmental SEM) and transmission electron microscopy, TEM (FEI Titan Themis 80-200). The energy-dispersive X-ray spectroscopy (EDS) analyzer attached to the FE-SEM was used to investigate the elemental composition.

Assembly of solid-state all pseudo-capacitive MoN@P-CF//RuO_2@CF asymmetric cell

Prior to assemble a full cell, MoN@P-CF and RuO_2@CF electrodes were tested in 1 M H_2SO_4 using 3-electrode configuration. In order to approach the highest cell voltage, the charges stored in positive and negative electrodes must be balanced by adjusting the mass loading of each of the active electrode materials. The capacitance of the MoN@P-CF (negative electrode) and RuO_2@CF (positive electrode) were balanced to satisfy $Q_+ = Q_-$.

$$\frac{m_{MoN}}{m_{RuO2}} = \frac{C_{RuO2} \times E_{RuO2}}{C_{MoN} \times E_{MoN}} = \frac{2}{1} \qquad (1)$$

The mass ratio of MoN@P-CF:RuO_2@CF was maintained to ~ 1:2. Thus, the total mass loading of active material in both electrodes was 3.4 mg/cm^2. The W_2N@P-CF//PPy@CF asymmetric device was assembled in coin cell design with 1 M H_2SO_4 electrolyte and a glass fiber separator.

The asymmetric cell was fabricated using MoN@P-CF as a negative electrode, RuO_2@CF as a positive electrode with PVA-H_2SO_4 gel as electrolyte and separator. PVA-H_2SO_4 gel-electrolyte was prepared by dissolving 3 g of PVA in 30 mL of deionized water at 70 °C under vigorous stirring for 60 min. After cooling down, 3 g of H_2SO_4 was added in the PVA solution and vigorously stirred for next 30 min to form a polymer gel-electrolyte. Now, both MoN@P-CF and RuO_2@CF electrodes were soaked in gel-electrolyte for 2 min and then dried at room temperature for 12 h to form a thin layer of the gel electrolyte on both the electrode. Finally, both the electrodes were pressed on each other to form flexible all pseudocapacitive solid-state MoN@P-CF and RuO_2@CF asymmetric cell.

Electrochemical Measurements

The electrochemical performances of individual electrodes and final asymmetric cells such as cyclic voltammetry (CV), galvanostatic charge/discharge (GCD) and electrochemical impedance (EIS) were conducted using a CHI760D electrochemical workstation. For three-electrode measurements, MoN@P-CF and RuO_2@CF electrodes were used as the working electrodes with platinum wire and Ag/AgCl as the counter and reference electrodes, respectively.

Calculations: Gravimetric (F/g) and areal specific capacitance (mF/cm^2) of electrode materials was calculated from the CD curves by integrating the discharge portion using the following equation:

$$C_s = \frac{I \times \Delta t}{m \times V} \; OR \quad C_A = \frac{I \times \Delta t}{A \times V} \qquad (2)$$

where *I* is the current (mA), *V* is the potential window (V) and *m* is the mass of the active material (mg).

Two-electrode configuration (cell measurements)

The areal (C_A) and volumetric (C_V) capacitance were estimated from the slope of the discharge curve using the following equations:

$$C_A = \frac{I \int V dt}{Area \times V^2} \quad OR \; C_A = \frac{I \int V dt}{Volume \times V^2} \qquad (3)$$

Where C_A and C_V are areal and volumetric capacitances, respectively. *I* is the applied current, *Δt* is the discharging time, *V* (V) is the voltage window, Volume (cm^3) of the whole device (The area and thickness of our asymmetric cells is about 0.785 cm^2 (Area, A=πr^2, 3.14 × (0.5)^2) and 0.088 cm. Hence, the whole volume of device is about 0.069 cm^3, *ΔV* (V) is the voltage window. It is worth mentioning that the volumetric capacitances were calculated taking into account the volume of the device stack. This includes the active material, the flexible substrate and the separator with electrolyte.

Volumetric energy (E, Wh/cm^3) and power density (P, W/cm^3) of the devices were obtained from the following equations:

$$E = \frac{1}{2 \times 3600} C_V \Delta V^2 \qquad (4)$$

$$P = \frac{3600 \times E}{\Delta t} \qquad (5)$$

where *E* (Wh/cm^3) is the energy density, C_V is the volumetric capacitance obtained from Equation (4) and *ΔV* (V) is the voltage window, P (W/cm^3) is the power density.

Electrochemical Impedance Calculations:

Furthermore, the capacitive behavior of device can also be evaluated from EIS technique by calculating the real and imaginary capacitance at a corresponding frequency using following equations:

$$C(\omega) = C^{'}(\omega) - jC^{''}(\omega) \quad (6)$$

Where,

$$C^{'}(\omega) = \frac{Z^{''}(\omega)}{\omega \mid Z(\omega) \mid^2} \quad (7)$$

$$C^{''}(\omega) = \frac{Z^{'}(\omega)}{\omega \mid Z(\omega) \mid^2} \quad (8)$$

where '*Z'* the complex impedance represented as $Z(\omega) = Z'(\omega) + Z''(\omega)$ and $\omega = 2\pi f$ where *f* is the frequency. $C'(\omega)$ is the real accessible capacitance of the electrode while $C''(\omega)$ is the energy loss due to the irreversible processes of the electrodes, Z' and Z'' are the real and imaginary parts of the Nyquist plot, respectively.

Density Functional Theory (DFT) computational details and models

All Density functional theory (DFT) simulations were carried out using the Vienna ab initio simulation package (VASP) (Kresse et al. 1993; Kresse et al. 1994) with the projector augmented wave pseudopotentials (PAW) (Blochl, 1994) and the periodic boundary conditions. The brillouin zone was sampled using 3 x 3 x 1 a Monkhorst-pack (Monkhorst and Pack, 1976) gamma centered mesh, and Gaussian smearing of 0.015 eV was used for the occupations of the electronic levels. Perdew-Burke-Ernzerhof (PBE) (Perdew et al. 1996; Perdew et al. 1997) functional within the generalized gradient approximation (GGA), was used to describe the electron interaction energy of exchange correlation. The electronic energies were converged within the limit of 10−7 ev and a cutoff of 600 ev was used. All geometries were optimized using 0.01 eV/Å force criteria. All the calculations were spin polarized. $H3O^+$ molecules were used to carry out all the proton adsorption calculations for CF, P-CF, MoN and their interfaces. The adsorption energy of proton within the supercells was calculated as follows:

$$E_{S@H3O} = E_{S@H3O} - [E_S + E_{H3O+}]$$

Where $E_{S@H3O}$ is the total energy of the substrate (Cf, P-CF, MoN@CF, MoN@P-CF) with the adsorbed H_3O^+, E_S is the total energy of a clean slab, and E_{H3O} is the energy of the hydronium cation. Through all the calculations, DFT+D3 approach developed by Grimme, was used for the long-range dispersion correction (Grimme et al. 2010).

For graphene fiber (CF) model, we have adopted 7 x 7 supercell (98 C atoms) and doped it with one and two phosphorus atoms which are corresponding to 1.0 at% and 2.0 at% of P:C, the latter is the

experimental atomic ratio (2.1 at%). We decide to use very large graphene layer and large vacuum distance of 20 Å in order to minimize the charge-image interactions. We have adopted P-sp3 type in our calculation because it reported as the most stable configuration of P-doped graphene system (P-CF) (Yang et al. 2017).

For MoN nanoparticles, we have modeled it using a 2 x 2 x 1 (100) slab of the hexagonal MoN (128 atoms) (Bull et al. 2004) and a thickness of 8 layer. Four of them were frozen and the upper four layers were relaxed. GGA+U formalism was used to describe the strong on-site coulomb interactions; we have adopted Dudraev et. al approach (Dudraev et al. 1998) which involves one parameter called the effective U (U-J, where U is the on-site coulomb repulsion and J is the on-site Hund exchange coupling. The U parameter was set to 3.0 ev in all our simulations involved MoN and the anti-ferromagnetic state used to describe the magnetism of the slab. The interfaces of MoN@CF and MoN@P-CF were generated using 6 x 6 x 1 of graphene sheet (CF, 72 atoms) and the above mentioned MoN slab. Here, we kept the doping ratio 1.4 at % for P-CF (which very near from of the experimental ratio 2.1 at%) to minimize the computational cost. The binding charge density was calculated using VESTA (Momma et al. 2011). Atom In Molecules (AIM) approach was used for the atomic charge analysis using bader code developed by henkelman group (Yu et al. 2011).

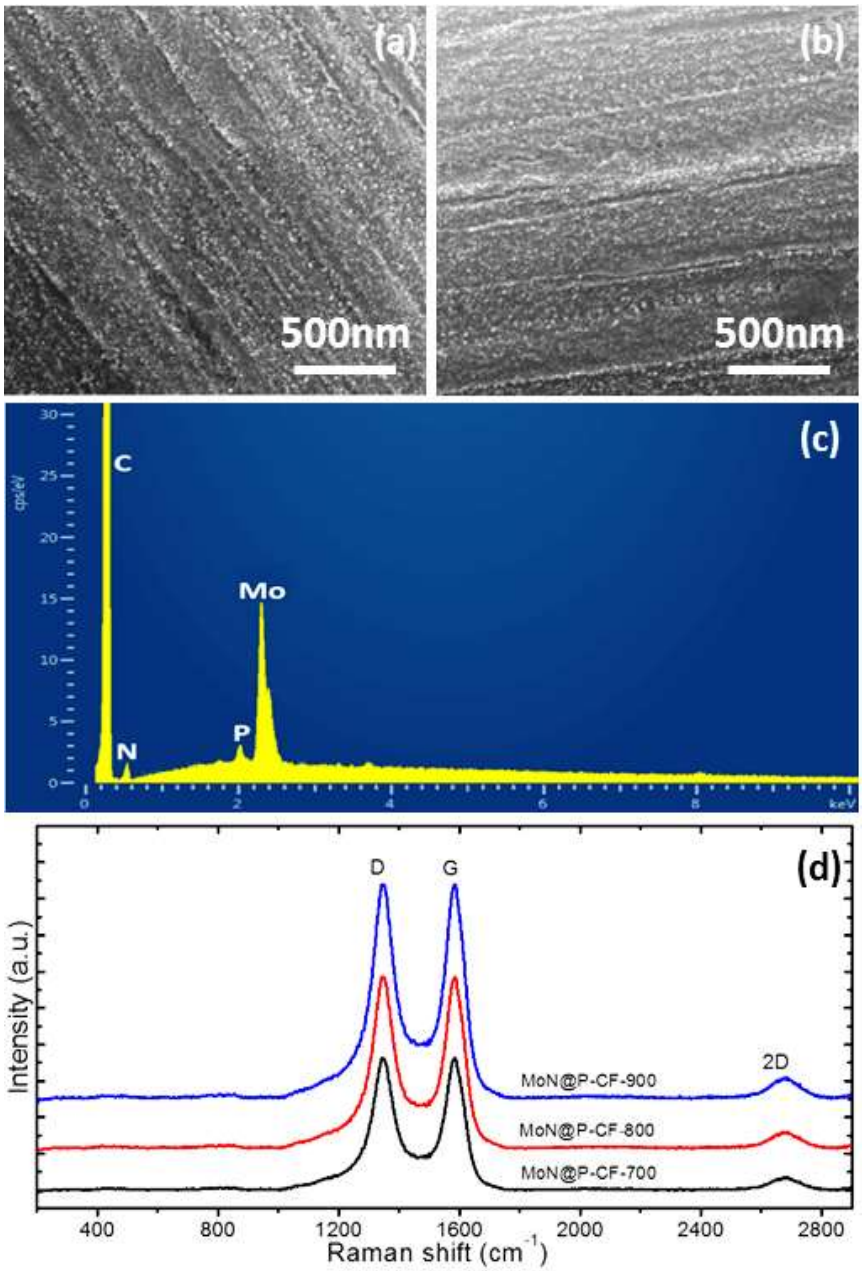

Figure S1 Characterizations of MoN@P-CF samples, Related to Figure 2. (a, b) SEM images of MoN@P-CF-700 and MoN@P-CF-800 samples, respectively. (c) EDAX pattern of MoN@P-CF-900 electrode, confirming the presence of Mo, N, C and P. (d) and (b) Raman spectra for MoN@P-CF samples prepared at different nitridation temperatures.

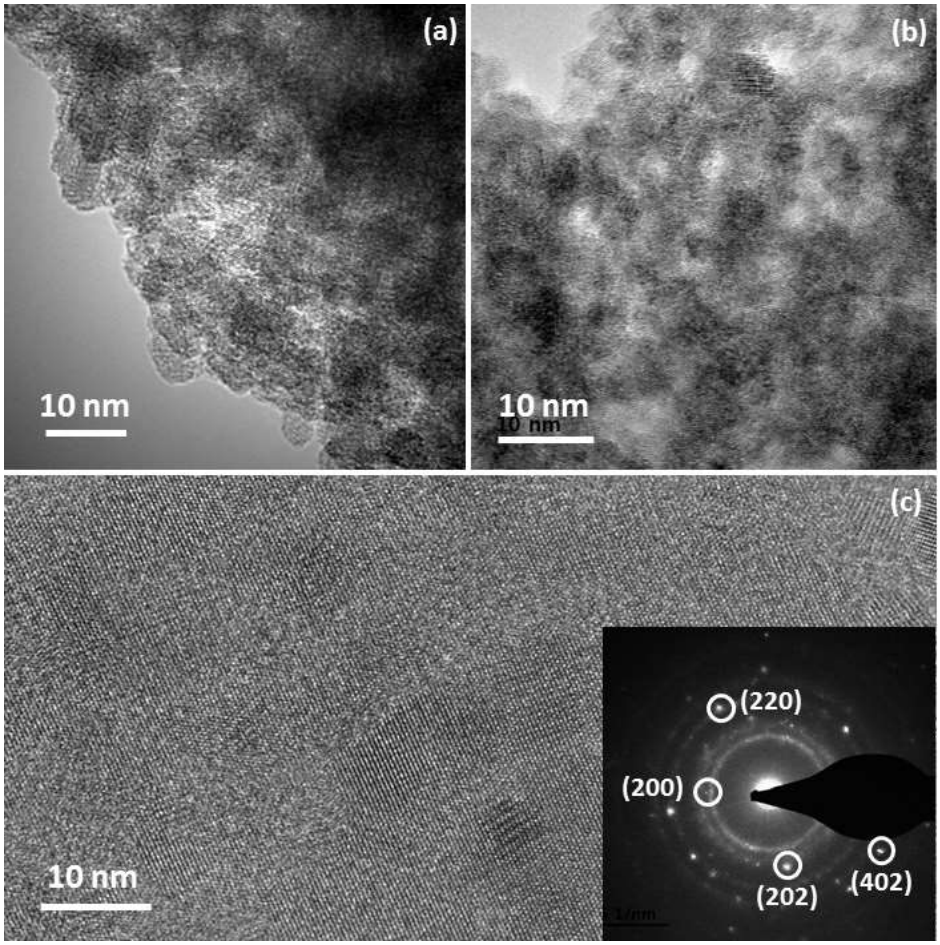

Figure S2 Characterizations of MoN@P-CF samples, Related to Figure 2. (a, b) TEM images for the MoN@P-CF sample prepared at 900 C, implying the formation of ultra-small MoN nanoparticle with the size less than 10 nm. (c) High magnified TEM image reveals that the MoN nanoparticles are crystalline in nature where distinct fringes can be clearly observed.

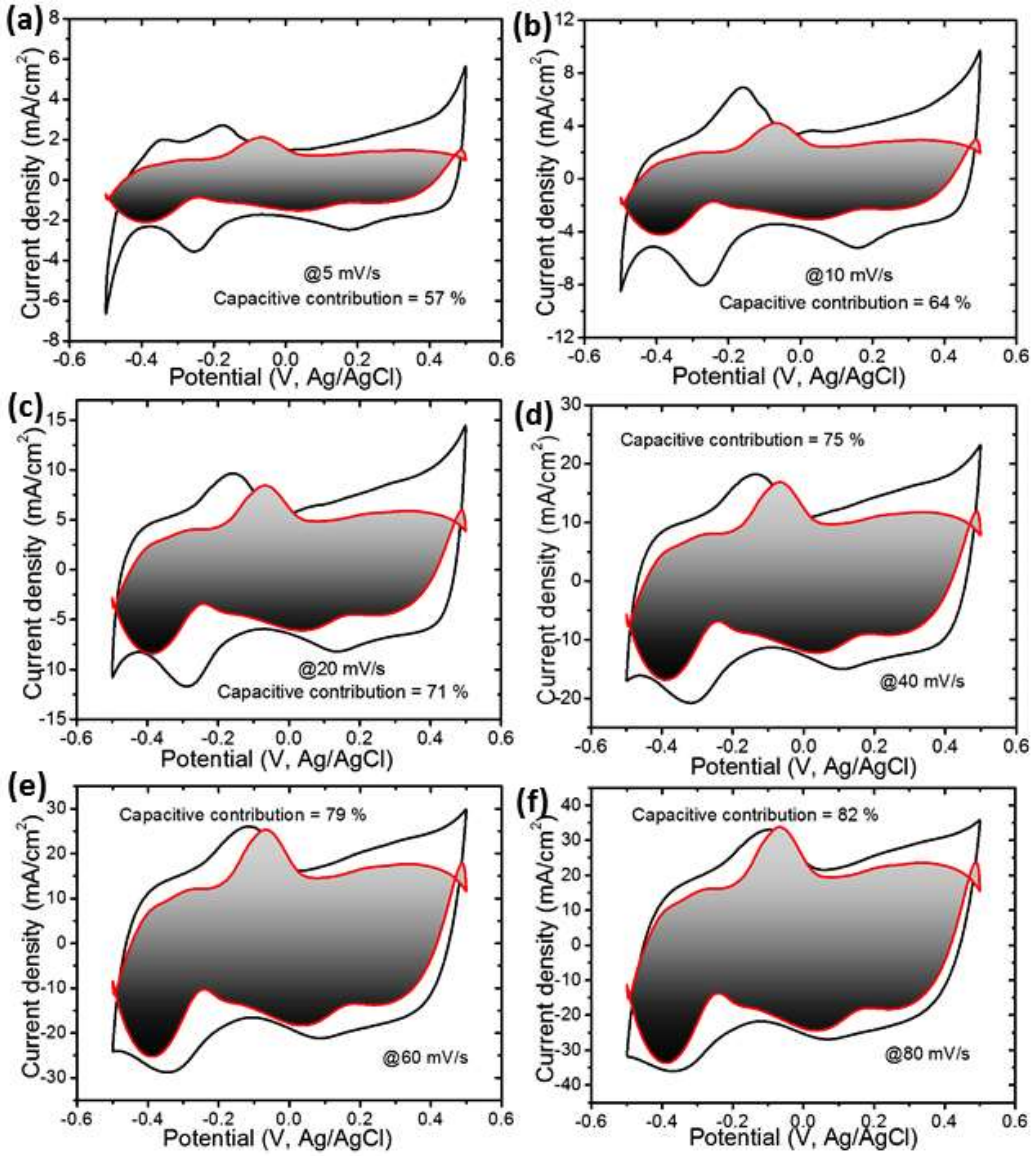

Figure S3 Electrochemical characterization of MoN@P-CF samples, Related to Figure 3. Cyclic voltammetry curves for MoN@P-CF-900 electrode at different scan rates from 10 to 100 mV/s. The capacitive contribution to the total current is shown by the shaded region.

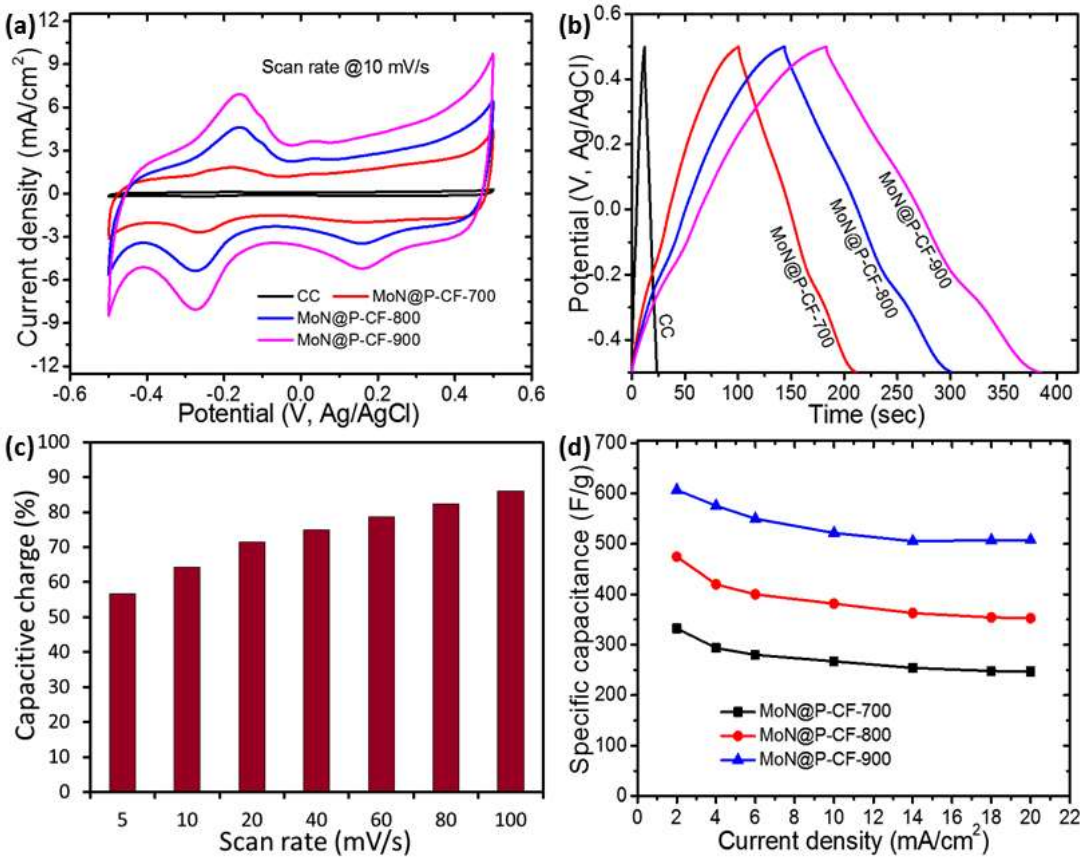

Figure S4 Electrochemical characterization of MoN@P-CF samples, Related to Figure 3. (a, b) Cyclic voltammetry and Galvanostatic CD curves recorded for MoN@P-CF samples prepared at different nitridation temperatures. (c) Variation of capacitive contribution with scan rate. (d) Variation of specific capacitance with current densities for different MoN@P-CF electrodes.

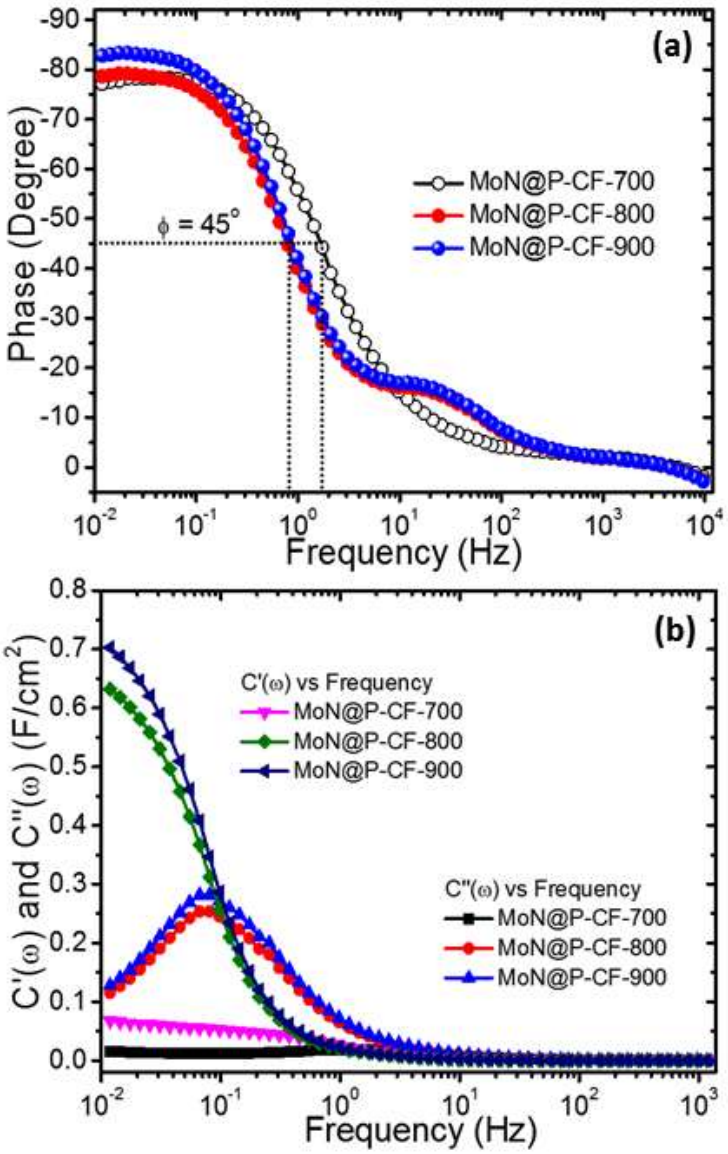

Figure S5 Electrochemical characterization of MoN@P-CF samples, Related to Figure 3. (a) Bode plots and (b) Real and imaginary capacitances with frequency for the MoN@P-CF samples prepared at different nitridation temperatures. The plot shows common relaxation-type dispersions where the real capacitance C' reduces with frequency while C'' shows maxima.

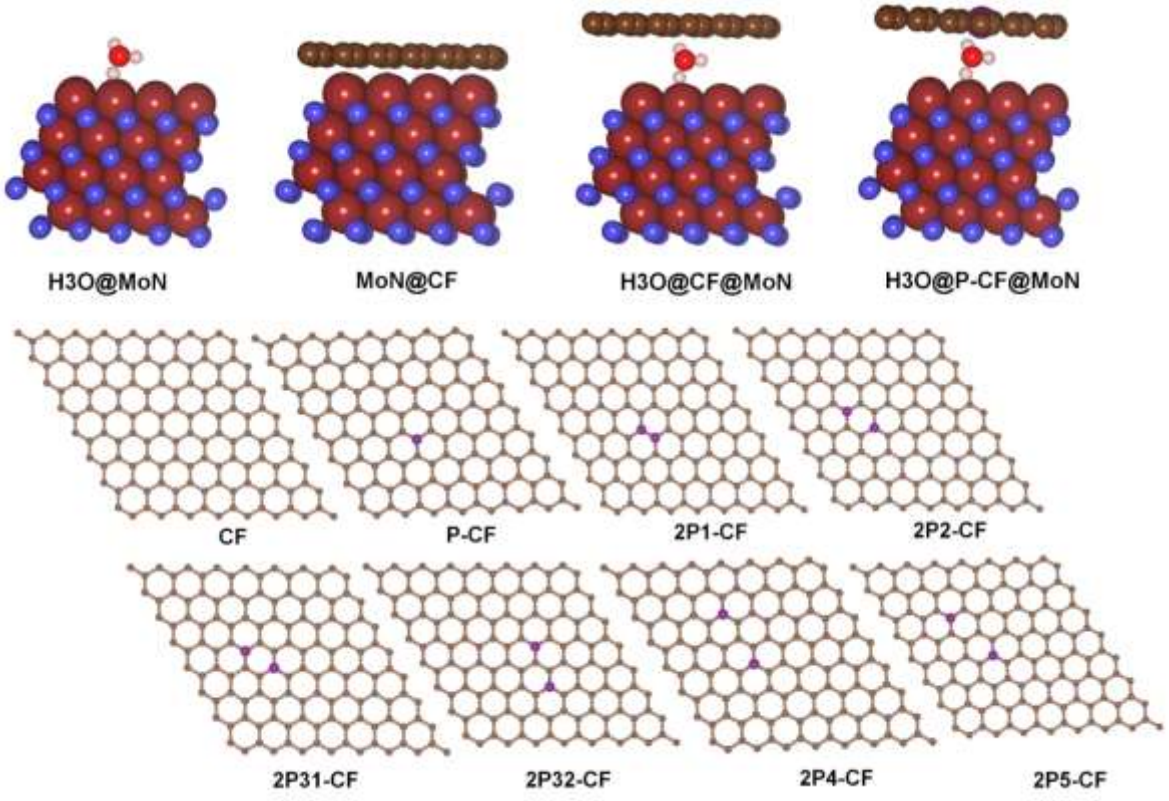

Figure S6 Initial Models of our DFT simulations of H3O+ adsorption on CF, P-CF, MoN, MoN@CF, and MoN@P-CF systems, Related to Figure 4. MoN, MoN@CF, MoN@P-CF, and H3O+ are represented by balls. Color code: MoN:plum, N:blue, C:brown, O:red, P:pink, and H:white. Isolated CF and P-CF models are shown in the lower panel and represented in balls and sticks. Different relative positions of the two phosphorus atoms (pink color spheres) are noted by Arabic numbers such as: P-CF, graphene sheet doped with one phosphorus, 2P1-CF is graphene doped by two phosphorus separated by one bond, 2P31-CF is graphene doped by two phosphorus and separated by two bonds and first configuration. The second Arabic letter after the phosphorus atom refers to the configuration numbers.

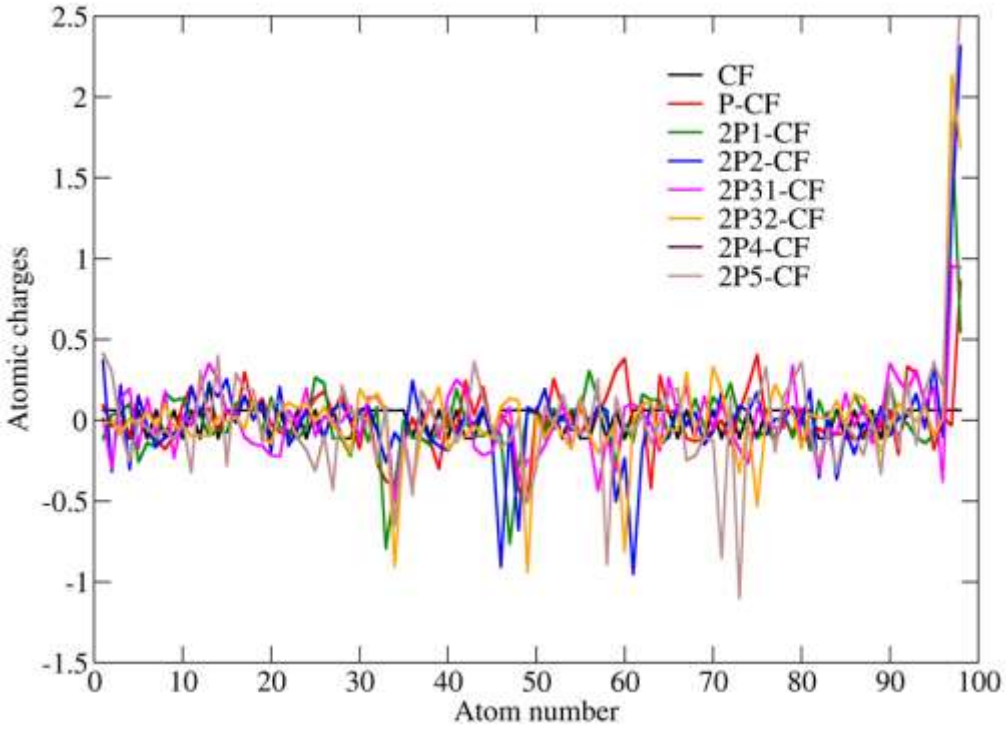

Figure S7 AIM atomic charges are shown for all CF and P-CF models, Related to Figure 4

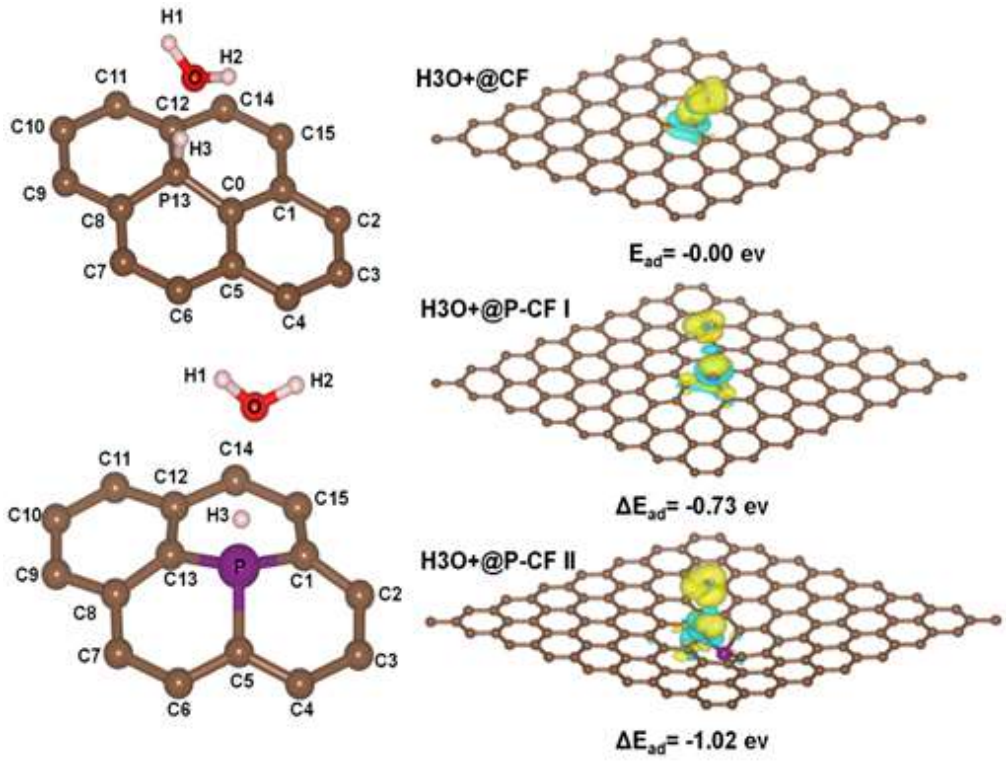

Figure S8 Binding charge densities of $H3O^+$ on the pristine CF and P-CF in two different mode of adsorption, **Related to Figure 4.** The isosurfaces is represented in resolution of 0.0025 electron/bohr3. Yellow is rich and blue is depletion of electron density. Left panel is showing the important carbon atoms surrounding the $H3O^+$ adsorption site in case of CF and P-CF I.

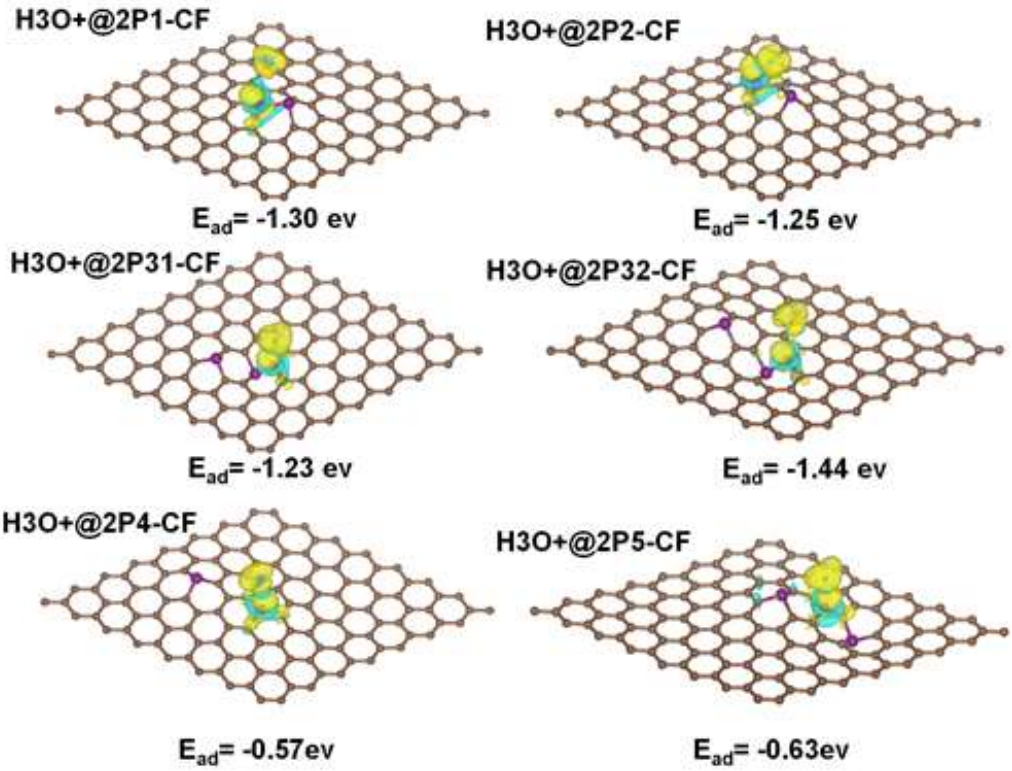

Figure S9: Binding charge densities of H3O+ on P-CF models following the same nomenclature reported in Figure S6, Related to Figure 4. The isosurfaces is represented in resolution of 0.015 electron/bohr3. Yellow is rich and blue is depletion of electron density.

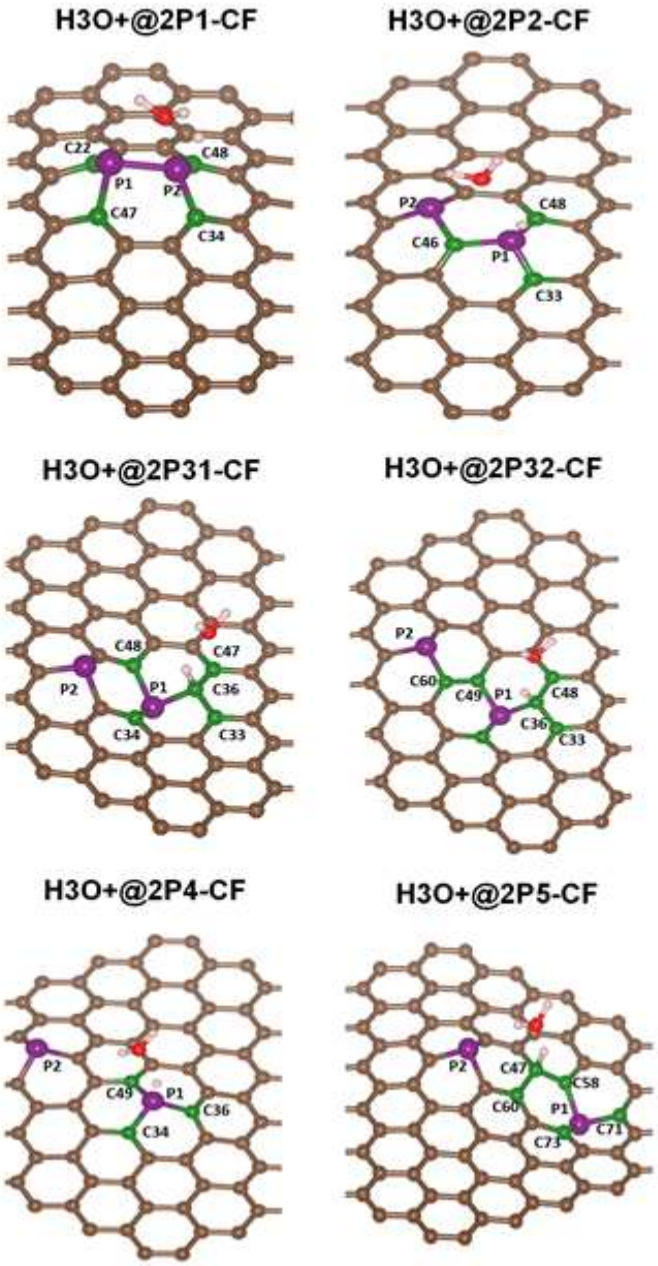

Figure S10 H3O+ binding sites of the P-CF considered systems depicted in Figure S9, Related to Figure 4. The important carbon atoms are colored in green the remaining is following the color code in Figure S6 and S9. The corresponding atomic charges are reported in Table S2.

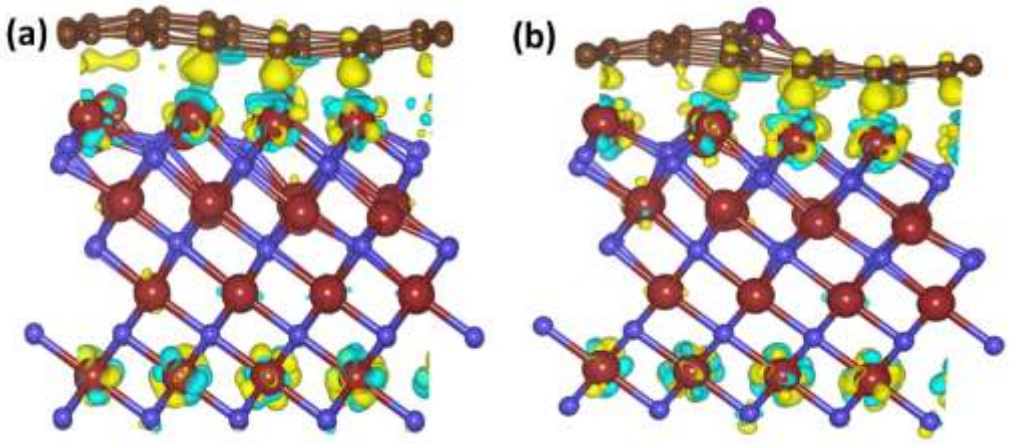

Figure S11 Charge density difference between the nano-composite MoN@CF, and MoN@P-CF, and their fragments (isolated slab, CF, and P-CF sheets), **Related to Figure 4**. The isosurfaces is represented in resolution of 0.015 electron/bohr3. Yellow is rich and blue is depletion of electron density. Color code is the same as in Figure S6.

RuO_2@CF: Film formation mechanism, Related to Figure 5.

The deposition of RuO_2 on the surface of carbon fabric (CF) was carried out using Layer-by-Layer method (LBL) by immersing CF in separately placed cationic and anionic precursors with rinsing between every immersion. The growth kinetics of the deposition process is based on ion-by-ion deposition at nucleation sites on the immersed surfaces.

In present investigation, RuO_2 were grown on the surface of CF through a controlled heterogeneous precipitation of $RuCl_3$. The proposed reaction mechanism is as follows: thin layer of Ru-species are adsorbed on the CF-substrate by immersion of the CF into the cationic precursor solution kept at room temperature (10 mM $RuCl_3$).

$$RuCl_3 + 3H_2O \rightarrow Ru(OH)_3^+ + 3HCl \qquad (9)$$

With further reaction is followed by the immersion of the wet substrate in H_2O_2 anionic solution, where the chemical reaction between oxygen species and pre-adsorbed Ru-species leads to the formation of thin layer of RuO_2 on the surface of CF.

$$2Ru(OH)_3^+ + H_2O_2 \rightarrow 2RuO_2 + 4H_2O \qquad (10)$$

This completes one cycle of deposition of RuO_2 at CF. We have performed different number of deposition cycles to obtain desired mass loadings.

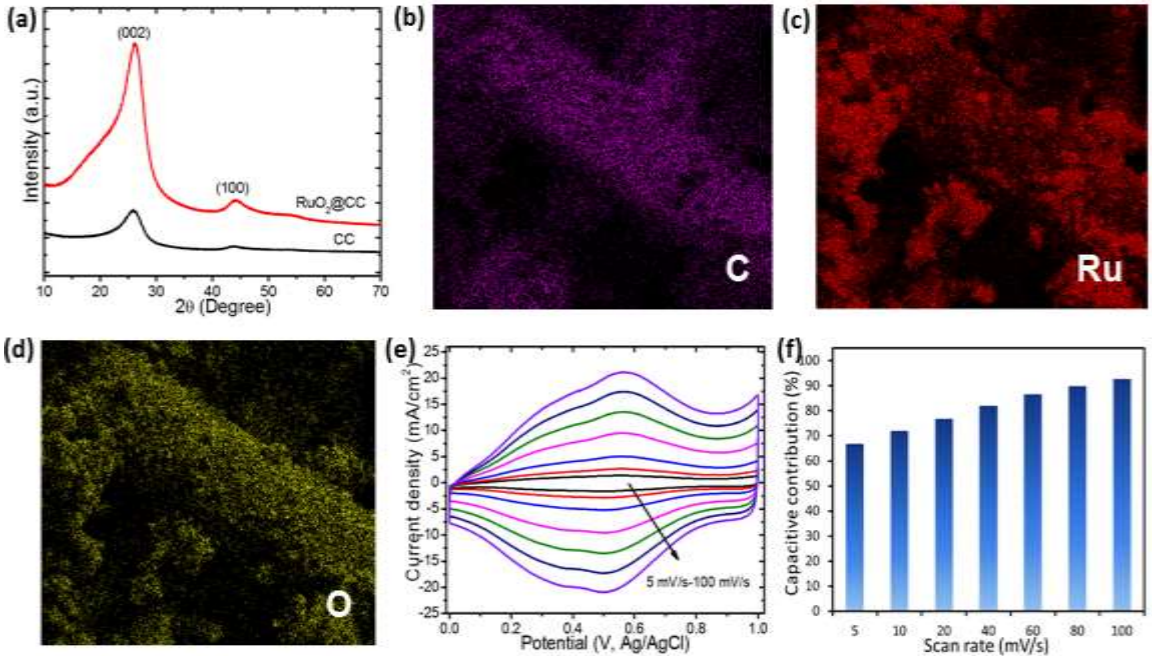

Figure S12 Characterizations of RuO_2@CF, Related to Figure 5. (a) XRD patterns of bare and RuO_2 coated carbon fabric electrodes. (b-d) EDS mapping images, displaying homogeneous coating of C, Ru and O, respectively. (e) CV curves measured at different scan rates in 1M H_2SO_4 electrolyte. (c) Plot of capacitive contribution as a function of scan rates.

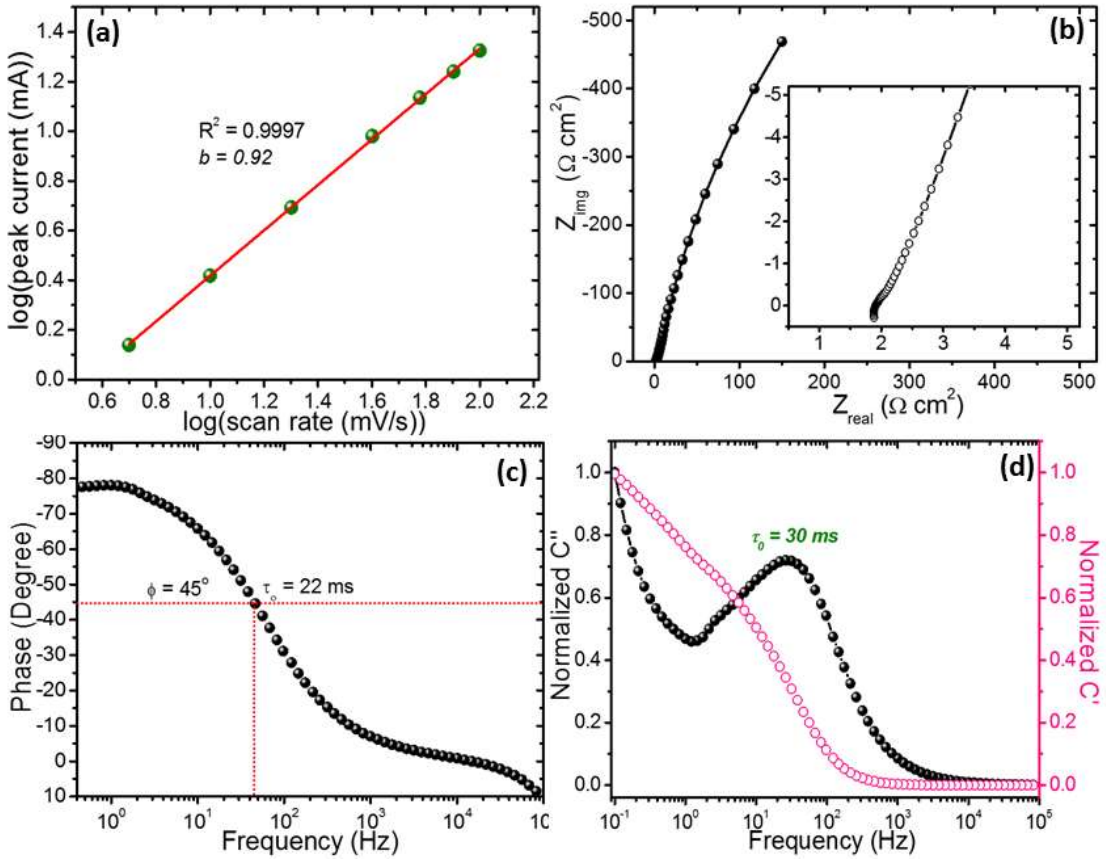

Figure S13 Electrochemical characterizations of RuO_2@CF, **Related to Figure 5**: (a) A plot of log (peak current, *i*) versus log(scan rate, mV/s), suggesting the major contribution to total current is from pseudocapacitive mechanism (b=0.92). (b) Nyquist plot recorded in the frequency range of 10 mHz to 100 kHz with amplitude of 5 mV. (c) Bode plots and (d) Real and imaginary capacitances with frequency, implying fast charge/discharge rates as relaxation time constant ($\tau_0 = 1/f_0$) was found to be 22-30 ms.

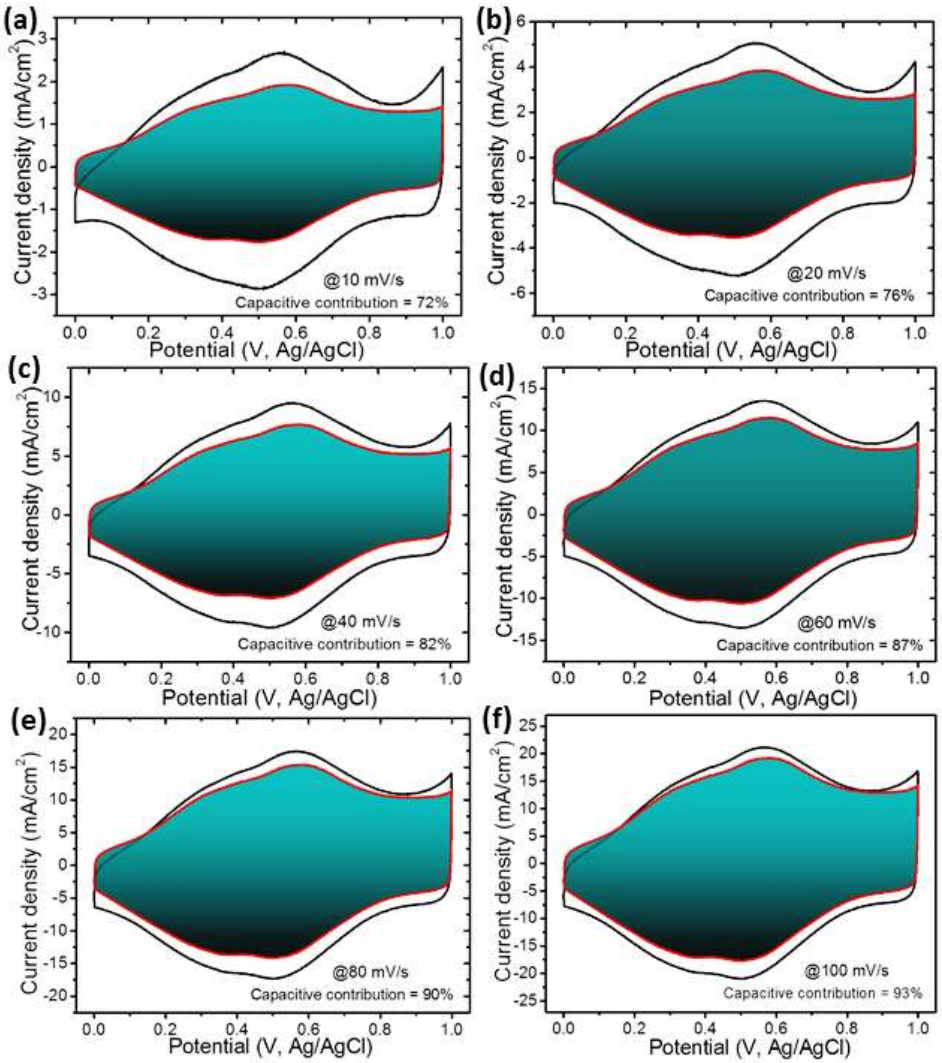

Figure S14 Electrochemical characterization of RuO_2@CF, Related to Figure 5. Cyclic voltammetry curves for RuO_2@CF electrode at different scan rates from 10 to 100 mV/s. The capacitive contribution to the total current is shown by the shaded region.

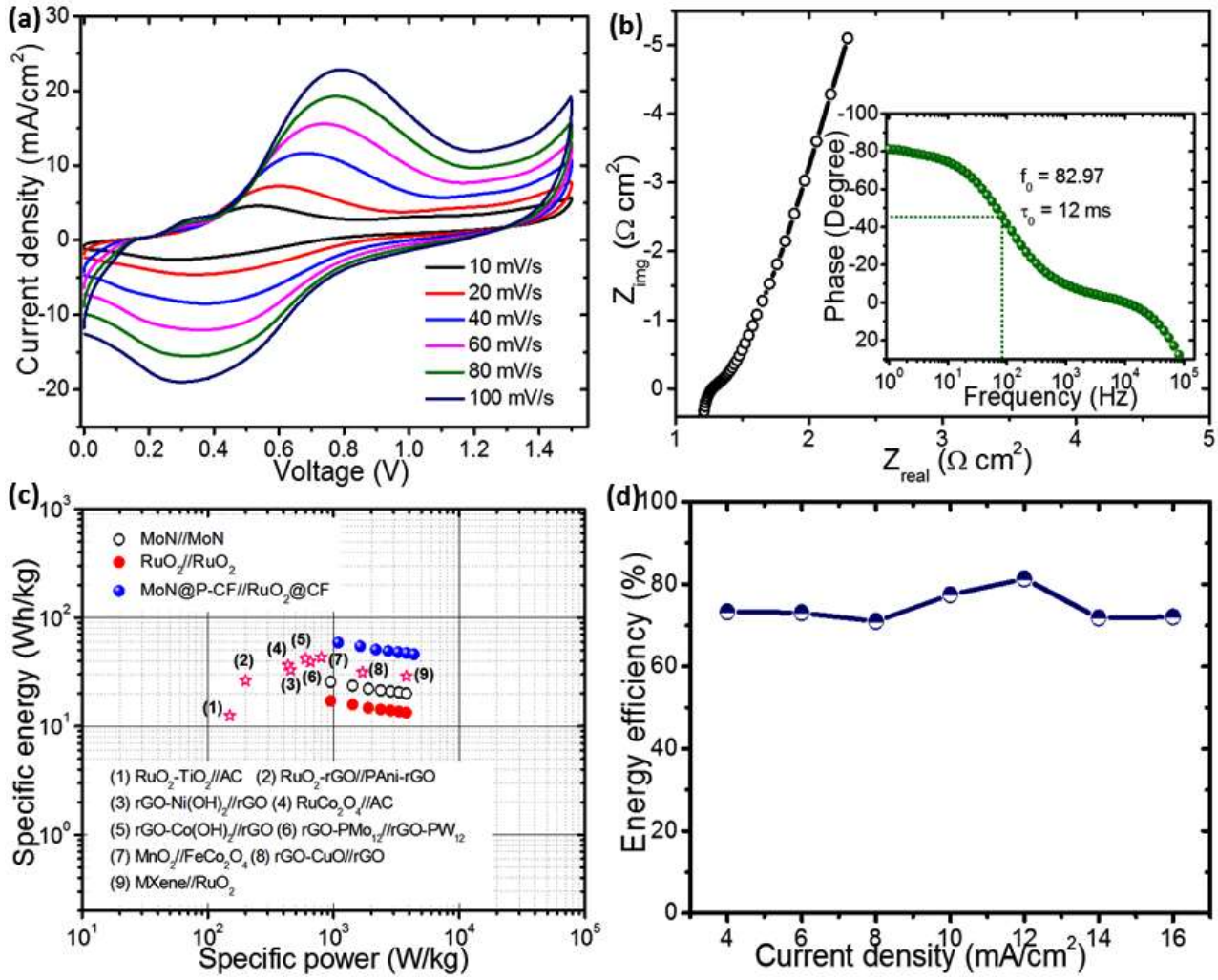

Figure 15 Electrochemical characterization of MoN@P-CF//RuO_2@CF cell, Related to Figure 6. (a) CV profiles for MoN@P-CF//RuO_2@CF asymmetric cell recorded at different scan rates. (b) Nyquist plot with their corresponding bode plot, confirming ultra-fast characteristics of the cell. (c) Ragone plot showing comparison of specific energy and specific power values with RuO2 based asymmetric systems. (d) Energy efficiency of device calculated at different current densities.

Table S1 Electrochemical performances of nitrides based electrodes for supercapacitor application, Related to Figure 3

Material	Electrolyte	Capacitance	Ref.
MoN@P-CF	1 M H_2SO_4	400 mF/cm^2 at 2 mA/cm^2	Present work
Molybdenum Oxynitride	1 M KOH	736.6 mF/cm^2 at 10 mV/s	Ruan et al. 2017
TiN	0.5 M H_2SO_4	27.3 mF/cm^2 at a current density of 1.0 mA/cm^2	Wei et al. 2018
CrN	0.5 M H_2SO_4	12.8 mF/cm^2 at 1.0 mA/cm^2	Wei et al. 2017
TiN	0.5 M K_2SO_4	8.8 mF/cm^2 at 100 mV/s	Achour et al. 2015
MoN	1 M H_2SO_4	928 F/cm^3 at 2 mV/s	Xiao et al. 2017
MoN	1 M KOH	130 mC/cm^2 at 2 mA/cm^2	Nandi et al. 2018
TiN	1 M H_2SO_4	10.9 mF/cm^2 at 0.1 V/s	Zheng et al. 2018
MoN_x/TiN	1 M LiOH	121.50 mF/cm^2 for at 0.3 mA/cm^2	Xie et al. 2017
Mo_2N	1 M H_2SO_4	172 F/g at 1 mV/s	Xue-liang et al. 2009
Mo_XN	4.4 M H_2SO_4	315 F/cm^3 at 10 mV/s	Roberson et al. 1999
Mo_2N	1 M H_2SO_4	171 F/g at 0.5 mA/cm^2	Zhang et al. 2016
Mo_3N_2	1 M KOH	220 F/g at 50 mV/s	Lee et al. 2013
Mo_2N	0.5 Li_2SO_4	722 F/cm^3 at 5 mV/s	Chen et al. 2017
Mo_2N	0.5 M K_2SO_4	275 F/g	Shah et al. 2014
Mo_2N@C-rGO	1 M H_2SO_4	514.54 F/g at 0.25 A/g	Sridhar et al. 2018
TiN@MoS_2	0.5 M H_2SO_4	662.2 mF/cm^2 at 1 mA/cm^2	Yu et al. 2017

Table S2 $H3O^+$ adsorption energies are reported referenced to the adsorption energy of CF pristine sheet. All energies are reported in electron volt (ev), Related to Figure 4.

Model	ΔE_{ads}
CF	0.0
P-CF	-1.02
2P1-CF	-1.30
2P2-CF	-1.25
2P31-CF	-1.23
2P32-CF	-1.44
2P4-CF	-0.57
2P5-CF	-0.63
MoN	-5.77
MoN@CF	-8.20
MoN@CF-P	-8.47

Table S3 Atomic charges are reported for H3O+ adsorption site in the three molecular models shown in Figure S7, Related to Figure 4

Atom	CF	P-CF I	P-CF II
C1	-0.028	-0.313	-0.414
C2	0.009	-0.073	0.002
C3	-0.082	0.171	0.062
C4	0.226	-0.114	-0.025
C5	0.172	-0.335	-0.439
C6	-0.150	-0.107	0.126
C7	-0.217	0.116	-0.057
C8	0.087	-0.013	0.139
C9	0.035	0.081	-0.044
C10	0.047	0.077	-0.142
C11	0.110	0.104	0.024
C12	0.194	-0.017	0.190
C13	-0.025	-0.294	-0.378
C14	-0.164	0.023	-0.091
C15	-0.270	-0.124	0.087
C0	0.0272	NA	NA
P	NA	1.125	1.121
O	-1.0396	-0.9587	-1.0241
H1	0.5356	0.5014	0.5365
H2	0.5562	0.5178	0.5320
H3	0.0589	-0.1945	0.0465

Table S4 Atomic charges are reported for complexes of H3O+ adsorbed on P-CF systems as depicted in Figure S9, Related to Figure 4 (Provided in Separate Excel sheet)

H_3O_+ adsorption on P-doped CF at 2%.

Results shown in S9, 10 and Table S4 can be explained based on the atomic charges reported in table S4 (excel sheet). The adsorption of H_3O^+ on 2P-CF fibers can be classified into two groups; the first group that display negative charges on the adsorbed proton as well as on adsorption site atoms (2P1-CF, 2P2-CF, and 2P4-CF) and the binding site is on P atoms. The second group has positive charge on the adsorbed proton and negative on the surrounding atoms (2P31-CF, 2P32-CF and 2P5-CF). The adsorption site of the latter group is on C atoms. In the first group, the repulsion between the adsorbed protons and the surrounding atoms decreases their stabilities, while the attractive forces induced by the positive charges on P atoms and the adsorbed proton balanced them. Their affinity is dependent on the distance between the two phosphorus atoms. In the second group, the situation is reversed, the attractive electrostatic forces between the adsorbed protons and the binding site atoms increased their stabilities while the repulsive forces with the positive charges on P atoms decrease them. The affinity of this group is also dependent on the distance between the binding site and the two P atoms.

Table S5 AIM atomic charges are reported for the complexes of H3O+ adsorbed on MoN, MoN@CF, and MoN@P-CF depicted in Figure S8. Related to Figure 4 (Provided in Separate Excel sheet)

Table S6 Comparison of electrochemical performances of MoN@P-CF//RuO_2@CF asymmetric supercapacitor cell, Related to Figure 6

Material used	Type of cell	Capacitance	Maximum Energy density	Maximum Power density	Stability	Ref.
MoN@P-CF//RuO_2@CF	Asymmetric cell	7.74 F/cm^3 at 4 mA/cm^2	2.4 mWh/cm^3	174 mW/cm^3	89 % over 15000 cycles	**Present work**
VOx//VN	Asymmetric cell	1.01 F/cm^3 (44.9 F/g) at 0.5 mA/cm^2	0.61 mWh/cm^3 at 0.5 mA/cm^2	0.85 W/cm^3 at 5 mA/cm^2	87.5 % over 10000 cycles	Lu et al. 2013
TiN@GNS//Fe_2N@GNS	Asymmetric cell	60 F/g at 4 A/g	0.51 mWh/cm^3 at 2 A/g	422.7 mW/cm^3 at 16 A/g	99.8% over 20000 cycles	Zhu et al. 2015
TiN/TiN	Symmetric cell	0.33 F/cm^3 at 2.5 mA/cm^3	0.05 mWh/cm^3 at 2.5 mA/cm^3	-	82 % over 15000 cycles	Lu et al. 2012
Mo_2N@rGO/ Mo_2N@rGO	Symmetric cell	15.4 F/cm^3 at 0.1 A/cm^3	1.05 mWh/cm^3 at 0.1 A/cm^3	3.15 W/cm^3 at 2 A/cm^3	85.7% over 4000 cycles	Ma et al. 2015
PANI//C/Mo_xN	asymmetric cell	65.2 F/g at 0.5 A/g	14.1 Wh/kg at 0.5 A/g	-	40.8 % over 3000 cycles	Tan et al. 2018
MnO_2/GNS// MoS_2/GNS	asymmetric cell	142 F/g (415 mF/cm^2 and 19.3 F/cm^3) at 2 mV/s	230.8 mWh/ cm^2 at	5.0 kW/kg	90 % over 5000 cycles	Yang et al. 2016
NiS/MoS_2//AC	asymmetric cell	108 F/g at 0.5 A/g	40 Wh/kg at 0.5 A/g	16.8 W/kg at 20 A/g	100 % over 10000 cycles	Yang et al. 2017b
MoS_2-NiO//MoS_2-Fe_2O_3	Asymmetric cell	-	39.6 Wh/kg at 1 A/g	-	95 % over 6000 cycles	Wang et al. 2017
RuO_2//Fe_2O_3	Asymmetric cell	54.5 mF/cm^2 at 0.13 mA/cm^2	1.5 mWh/ cm^3 at 0.13 mA/cm^2	-	97 % over 5000 cycles	Wang et al. 2018

Supplemental References

Achour, A., Porto, R., Soussou, M., Islam, M., Boujtit, M., Aissa, K., Brizoual, L., Djouadi, A., Brousse, T. (2015). Titanium nitride films for micro-supercapacitors: Effect of surface chemistry and film morphology on the capacitance J. Power Sources 300, 525-532.

Blochl. P. E. (1994). Projector augmented-wave method. Phys. Rev. B, 50, 17953.

Bull, C. L., McMillan, P. F., Soignard, E., Leinenweber, K. (2004) Determination of the crystal structure of δ-MoN by neutron diffraction. J. Solid State Chem., *177*, 1488–1492

Chen, L., Liu, C., Zhang, Z. (2017). Novel [111] oriented γ-Mo_2N thin films deposited by magnetron sputtering as an anode for aqueous micro-supercapacitors. Electrochimica Acta 245, 237–248.

Dudarev, S. L., Botton, G. A., Savrasov, S. Y., Humphreys, C. J., Sutton, A. P. (1998). Electron-energy-loss spectra and the structural stability of nickel oxide:An LSDA1U study. Phys. Rev. B 57, 1505–1509.

Grimme, S., Antony, J., Ehrlich, S., Krieg, H. (2010). A consistent and accurate ab initio parametrization of density functional dispersion correction (DFT–D) for the 94 elements H–Pu. J. Chem. Phys. 132, 154104.

Kresse, G., Hafner, J. (1993). Ab initio molecular dynamics for liquid metals. Phys. Rev. B, 47, 558

Kresse, G., Hafner, J. (1994). Ab initio molecular-dynamics simulation of the liquid-metal-amorphous-semiconductor transition in germanium. Phys. Rev. B, 49, 14251.

Lee, K., Lee, Y., Ko, A., Cao, G., Park, K. (2013). Single-crystalline mesoporous molybdenum nitride nanowires with improved electrochemical properties. J. Am. Ceram. Soc., 96, 37–39.

Lu, X., Wang, G., Zhai, T., Yu, M., Xie, S., Ling, Y., Liang, C., Tong, Y., Li, Y. (2012). Stabilized TiN nanowire arrays for high-performance and flexible supercapacitors. Nano Lett. 12, 5376−5381.

Lu, X., Yu, M., Zhai, T., Wang, G., Xie, S., Liu, T., Liang, C., Tong, Y., Li, Y. (2013) High energy density asymmetric quasi-solid-state supercapacitor based on porous vanadium nitride nanowire anode. Nano Lett. 13, 2628-2633.

Monkhorst, H., Pack, J. (1976). Special points for Brillouin–zone integrations. Phys. Rev. B 13, 5188-5192.

Momma, K., Izumi, F. (2011). VESTA 3 for three-dimensional visualization of crystal, volumetric and morphology data. J. Appl. Crystallogr., 44**,** 1272-1276.

Ma, G., Wang, Z., Gao, B., Ding, T., Zhong, Q., Peng, X., Su, J., Hu, B., Yuan, L., Chu, P., Zhou, J., Huo, K. (2015). Multilayered paper-like electrodes composed of alternating stacked mesoporous Mo2N nanobelts and reduced graphene oxide for flexible all-solid-state supercapacitors. J. Mater. Chem. A, 3, 14617–14624.

Nandi, D. K., Sahoo, S., Kim, T. H., Cheon, T., Sinha, S., Rahul, R., Jang, Y., Bae, J., Heo, J., Shim, J., Kim, S. (2018). Low temperature atomic layer deposited molybdenum nitride-Ni-foam composite: An electrode for efficient charge storage. Electrochem. Commun. 93, 114–118.

Perdew, J. P., Burke, K. , Ernzerhof, M. (1996) Generalized gradient approximation made simple. Phys. Rev. Lett., 77, 3865.

Perdew, J. P., Burke, K. , Ernzerhof, M. (1997) Erratum: Generalized gradient approximation made simple. Phys. Rev. Lett., 78, 1396.

Ruan, D., Lin, R., Jiang, K., Yu, X., Zhu, Y., Fu, Y., Wang, Z., Yan, H., Mai, W. (2017). High-Performance Porous Molybdenum Oxynitride Based Fiber Supercapacitors. ACS Appl. Mater. Interfaces, 9, 29699-29706.

Roberson, S. L., Finello, D., Davis, R. F. (1999). Electrochemical evaluation of molybdenum nitride electrodes in H2SO4 electrolyte. J. Appl. Electrochem., 29, 75-80.

Shah, S., Hector, A., Owen, J., (2014). Redox supercapacitor performance of nanocrystalline molybdenum nitrides obtained by ammonolysis of chloride-and amide-derived precursors. J. Power Sources 266, 456-463.

Sridhar, V., Park, H. (2018). Carbon sheathed molybdenum nitride nanoparticles anchored on reduced graphene oxide as high-capacity sodium-ion battery anodes and supercapacitors. New J. Chem., 42, 5668-5673.

Tan, Y., Meng, L., Wang, Y., Dong, W., Kong, L., Kang, L., Ran, F. (2018). Negative electrode materials of molybdenum nitride/N-doped carbon nano-fiber via electrospinning method for high-performance supercapacitors. Electrochimica Acta 277, 41-49.

Wei, B., Liang, H., Zhang, D., Qi, Z., Shen, H., Wang, Z. (2018). Magnetron sputtered TiN thin films toward enhanced performance supercapacitor electrodes. Mater Renew Sustain Energy 7, 11.

Wei, B., Liang, H., Zhang, D., Wu, Z., Qi, Z., Wang, Z. (2017). CrN thin films prepared by reactive DC magnetron sputtering for symmetric supercapacitors. J. Mater. Chem. A 5, 2844-2851.

Wang, K., Yang, J., Zhu, J., Li, L., Liu, Y., Zhang, C., Liu, T. (2017) General solution-processed formation of porous transition-metal oxides on exfoliated molybdenum disulfides for high-performance asymmetric supercapacitors. J. Mater. Chem. A, 5, 11236-11245.

Wang, Q., Liang, X., Ma, Y., Zhang, D. (2018). Fabrication of hollow nanorod electrodes based on RuO2//Fe 2 O 3 for an asymmetric supercapacitor. Dalton Trans., 47, 7747–7753.

Xie, Y., Tian, F. (2017). Capacitive performance of molybdenum nitride/titanium nitride nanotube array for supercapacitor. Mater. Sci. Eng. B 215, 64–70

Xue-liang, L., Yan, X., Hua, W., Hua-lin, W., Wei-dong, W., Xiang-ying, C. (2009) Synthesis and characterization of uniform nanoparticles of γ-Mo2N for supercapacitors. Trans. Nonferrous Met. Soc. China 19, 620-625.

Xiao, X., Yu, H., Jin, H., Wu, M., Fang, Y., Sun, J., Hu, Z., Li, T., Wu, J., Huang, L., Gogotsi, Y., Zhou, J. (2017). Salt-Templated Synthesis of 2D Metallic MoN and Other Nitrides. ACS Nano 11, 2180-2186.

Yang, X., Niu, H., Jiang, H., Wang, Q., Qu, F. (2016). A high energy density all-solid-state asymmetric supercapacitor based on MoS2/graphene nanosheets and MnO2/graphene hybrid electrodes. J. Mater. Chem. A, 4, 11264–11275.

Yang, N., Zheng, X., Li, L., Li, J., Wei, Z., (2017). Influence of Phosphorus Configuration on Electronic Structure and Oxygen Reduction Reactions of Phosphorus-Doped Graphene, J. Phys. Chem. C, 121, 19321-19328.

Yang, X., Zhao, L., Lian, J. (2017). Arrays of hierarchical nickel sulfides/Mo2 nanosheets supported on carbon nanotubes backbone as advanced anode materials for asymmetric supercapacitor. J. Power Sources 343, 373-382.

Yu, M., Trinkle, D. R. (2011) Accurate and efficient algorithm for Bader charge integration, J. Chem. Phys. 134, 064111.

Yu, M., Zhao, S., Feng, H., Hu, L., Zhang, X., Zeng, Y., Tong, Y., Lu, X. (2017). Engineering Thin MoS_2 Nanosheets on TiN Nanorods: Advanced Electrochemical Capacitor Electrode and Hydrogen Evolution Electrocatalyst. ACS Energy Lett. 2, 1862−1868.

Zhang, W., Ma, X., Kong, L., Liu, M., Luo, Y., Kang, L. (2016). Electrochemical performance of pseudo-capacitive intermetallic molybdenum nitride in acid. J. Electrochem. Soc., 163, A1300-A1305.

Zheng, T., Tahmasebi, M., Li, B., Li, Y., Ran, S., Glen, T., Lam, K., Choi, I., Boles, S. (2018). Sputtered Titanium Nitride Films on Titanium Foam Substrates as Electrodes for High-Power Electrochemical Capacitors. ChemElectroChem 5, 2199-2207.

Zhu, C., Yang, P., Chao, D., Wang, X., Zhang, X., Chen, S., Tay, B., Huang, H., Zhang, H., Mai, W., Fan, H. (2015). All Metal Nitrides Solid-State Asymmetric Supercapacitors. Adv. Mater., 27, 4566–4571.